Title

Hydro-Mechanical Measurements of Sheared Crystalline Rock Fractures With Applications for EGS Collab Experiments 1 and 2

Journal

Journal of Geophysical Research: Solid Earth, 127(2)

ISSN

2169-9313

Authors

Meng, Meng
Frash, Luke P
Li, Wenfeng
et al.

Publication Date

2022-02-01

DOI

10.1029/2021jb023000

Peer reviewed

Title: Hydro-mechanical measurements of sheared crystalline rock fractures with applications for EGS Collab experiments 1 and 2

Authors: Meng Meng[1*], Luke P. Frash[1], Wenfeng Li[1], Nathan J. Welch[1], J. William Carey[1], Joseph Morris[2], Ghanashyam Neupane[3], Craig Ulrich[4], Timothy Kneafsey[4]

Affiliations:

[1]Los Alamos National Laboratory, Los Alamos, New Mexico, USA

[2]Lawrence Livemore National Laboratory, Livermore, California, USA

[3]Idaho National Laboratory, Berkeley, Idaho Falls, Idaho, USA

[4]Lawrence Berkeley National Laboratory, Berkeley, California, USA

[*]Corresponding author: Meng Meng (mengm@lanl.gov)

Key Points

- Hydroshearing requires a natural fracture that is mechanically weak, hydraulically conductive, and favorably oriented.
- Fracture shear slip does not always result in permeability enhancement; when phyllosilicate rich, we observed decreasing permeability.
- Slip-tendency analysis improved by hydro-mechanical measurement helps to select the best candidate fracture for hydroshearing in the field.

Abstract

We present hydro-mechanical measurements that characterize shear on natural fractures in schist, amphibolite, and rhyolite specimens from the EGS Collab Project's Experiment 1 and 2 sites (E1 and E2) at the Sanford Underground Research Facility (SURF). We employed a triaxial direct shear method augmented with x-ray imaging to perform hydroshearing (injection-induced shearing) and mechanical shearing on naturally fractured specimens at in-situ stress conditions. Measurements included fracture permeability, strength, stress-dependent aperture, shear dilation, and frictional strength. Results reveal that in situ natural fractures must be permeable, weak, and shear-oriented to be hydrosheared, and only a subset of the observable in-situ fractures were suitable. When sheared, the fracture permeability typically increased by a factor of 10 or more and this increase was retained over time. However, shear slip did not always result in permeability increase. High phyllosilicate content associated with exceptionally weak fractures exhibited poor or even decreased permeability after stimulation. These measurements in combination with site data were used to conduct a slip-tendency analysis for different fracture sets, and we selected the top candidate natural fractures for hydroshearing at the EGS Collab sites. We also found that the lower in-situ shear stress and stronger fractures at the E2 site make hydroshearing more challenging than at the E1 site. Overall, the methods and analysis used in our work can be applied to any geothermal project to identify in-situ joint sets that are best suited for hydroshearing, which in turn can help to optimize well placement and energy production.

Keywords: triaxial direct shear; hydroshearing; enhanced geothermal systems; permeability; faults

Plain Language

Geothermal energy is attractive because it is green, clean, and 'always on'. However, technical challenges and high-capital costs historically hindered its development. Among the technical challenges, is a need to reliably increase the rock permeability to promote productive geothermal wells. One leading method is called "hydroshearing", where fluid is injected to encourage shear slip along pre-existing natural fractures and thus open the fractures to increase permeability. Our research focuses on the EGS Collab Project's field sites where we characterize actual natural fractures so that we can predict shear slip via hydroshearing and then identify the best locations for drilling wells suitable for hydroshearing. This work included measuring

a suite of coupled hydraulic and mechanical properties for crystalline geothermal rocks drilled from this field site. We demonstrate that pre-existing natural fractures must be mechanically weak, favorably oriented, and sufficiently permeable to be hydrosheared. Combining measured in-situ stresses with natural fractures properties, we were able to identify suitable natural fractures for hydroshearing and to better optimize well design at the EGS Collab sites. This positive outcome from our work could be similarly applied to full-scale geothermal systems to improve well productivity, reduce the risk of failed wells, and to improve economics.

1 Introduction

Geothermal energy is attractive because it helps secure energy supply, mitigate climate change, and comply with future green energy policies. The GeoVision study estimates a potential 26-fold increase from 2019 geothermal energy production levels to 60 GW by 2050 in the United States (Hamm et al., 2019; Bromley et al., 2010; Dobson et al., 2017; Fan, 2020). To expand geothermal energy production, enhanced geothermal system (EGS) is a key candidate technology (Tester et al., 2006). Hydraulic fracturing is a stimulation method for EGS, where high injection pressures are used to create tensile fractures. Hydroshearing is another closely related stimulation method where fluid injection increases pore pressures and then triggers slip along pre-existing fractures. Both hydroshearing and hydraulic fracturing are essential process for enhancing rock permeability to create successful EGS (McClure and Horne, 2014a). However, fracture shear slip and its effects are challenging to predict for a given site.

Characterizing shear slip on natural fractures and faults can better inform predictions of natural or induced seismicity (Hincks et al., 2018), fault stability (Marone and Kilgore, 1993), and stimulated fracture fluid conductivity (Frash et al., 2017). Prior works have investigated frictional strength for stick-slip behavior (Leeman et al., 2016), permeability evolution during earthquake slip (Im et al., 2018), fault weakening induced by fluid injection (Scuderi et al., 2017), and scaling relations from shear fractures measured in the laboratory to the larger field situation (Pyrak-Nolte and Morris, 2000; Schultz et al., 2008; Frash et al., 2019a; Wenning et al., 2019, 2021). Accurate site-specific characterization of shear fractures is especially important for geothermal energy applications where it is hoped that shear-propping (McClure and Horne, 2014b) could be a good alternative to the conventional proppants that are expected to perform poorly at high-stress and high-temperature conditions (Brinton, 2011).

The crystalline and sedimentary rock that constitute most geothermal reservoirs are characterized by low permeability but often contain natural fractures (Dezayes et al., 2010). In this environment, conductive fractures are the dominant mechanism for fluid flow and heat extraction. The EGS Collab Project is investigating fracture-dominated high-stress crystalline-rock fluid-flow and the associated geophysical signatures using decameter scale (~10m) hydraulic stimulation experiments at Sanford Underground

Research Facility (SURF) in South Dakota. This effort contributes to solving the above challenges as well as supporting future full-scale experiments at the Frontier Observatory for Research in Geothermal Energy (FORGE) in Milford, Utah. The EGS Collab project field sites include Experiment 1 (E1) at 1480 m depth and Experiment 2 (E2) at 1250 m. To assist the field scale hydraulic stimulation experiments and improve understanding of EGS design, the laboratory work is needed to better understand the mechanisms of fluid flow and hydroshearing potentials for those nature fractures in the field.

A variety of test methods were applied in the prior work, including direct shear, triaxial direct shear, triaxial compression, and triaxial punch-through shear. Table S1 in the Supplementary Information summarizes prior experimental studies on shear fractures. Most researchers found the permeability of granite can be increased by one to three orders of magnitude after shear (Gentier et al., 1997; Esaki et al., 1999; Zhang et al., 2019; Chen et al., 2020). However, there are differences as to where this enhancement persisted (Witherspoon et al., 1980; Kluge et al., 2020; Ye and Ghassemi, 2018) or was lost (Nemoto et al., 2008; Bauer et al., 2016). Recent findings showed that the fracture roughness strongly influences hydro-mechanical properties (Ye and Ghassemi, 2018; Acosta et al., 2020). However, most work that studied shear fracture properties, apart from Mitchell and Faulkner (2008) and Kluge et al. (2020, 2021), used either saw-cut or a tensile splitting method, to produce planar to sub-planar fracture segments for experiments. We note that manufactured fractures may not replicate the natural rough fractures in the subsurface that have complex and heterogeneous structures including curvature, en échelon structures, stranding, damaged fracture surfaces, gouge and chemical infilling (Rutqvist et al., 2018; Frash et al., 2019a). For the two studies that used in-situ created fractures (Mitchell and Faulkner 2008; Kluge et al., 2020, 2021), hydroshearing was not performed, and the hydro-mechanical behavior was tested only by mechanical shear. Furthermore, most studies only focused on granite, some studies lack permeability measurements, and few make hydroshearing measurements. The EGS Collab field sites include naturally fractured schist, amphibolite, and rhyolite (Roggenthen, 2017; Kneafsey et al., 2019; Singh et al., 2019). None of the prior research studied hydroshearing or coupled hydro-mechanical properties for natural fractures through these crystalline rocks, so our work is the first to do so.

To better understand the fundamental mechanisms of fracture fluid flow and best assist the EGS Collab Project's hydroshearing stimulation design, we determined that the test should include: (1) direct flow through the fracture that does not require in-series matrix diffusion; (2) stimulation of fractures at desired representative subsurface conditions while simultaneously measuring permeability; (3) hydroshearing attempts in the laboratory at replicated field stress conditions; (4) simultaneous mechanical, hydraulic, and geometry measurement without unloading; and (5) targeting the EGS Collab's natural fractures obtained from subsurface cores. In previous studies, only (1) and (2) were met. Some researchers (Nemoto et al.,

2008; Bauer et al., 2016; Ye and Ghassemi, 2019, 2020) made significant contributions to exploring mechanisms of hydroshearing, but these can't be readily applied to site-specific conditions. In effect, EGS Collab provided a rare opportunity to combine site-specific measurements on targeted natural fractures to inform decision-making to design wells and future hydraulic stimulations.

To satisfy the above test requirements (1 to 6), we conduct triaxial direct-shear experiments with integrated real-time x-ray computed tomography (CT) on natural fractures in crystalline rock collected intact from EGS Collab core with measurements of fracture reactivation, displacement and permeability among other geomechanical parameters. Our study has two primary goals. First, characterize the hydro-mechanical properties of natural fractures at the EGS Collab Project's two sites, E1 and E2. This provides key inputs for field-scale multiphysics simulations of geothermal energy extraction. Second, evaluate the implications of these measurements (fracture strength and permeability) for predicting hydroshearing conditions for the natural fractures at each site. This helps to identify in-situ joint sets that are best suited for hydroshearing and optimize well placement in the field.

2 Experimental Methods

2.1 Specimen Preparation

Our specimens were cored from the EGS Collab sites on the 4100 and 4850 levels of SURF, at depths of 1250 m (E2) and 1480 m (E1), respectively. All test specimens were prepared as right-regular cylinders with a nominal length of 25 mm and diameter of 25 mm. Two groups of field stimulation experiments were originally planned. Experiment 1 (E1) focused on hydraulic fracturing and the forthcoming Experiment 2 (E2) is being designed to promote hydroshearing. The E2 site is located in the carbonate-rich, quartz-bearing phyllite of the upper Poorman schist (PS01 specimens), whereas the E1 site is located in the Yates amphibolite with rhyolite intrusions (YA02 specimens). Both sites were previously characterized for natural fracture locations, orientations, and state of stress by Ulrich et al. (2018), and is summarized in Table 1.

Geologically, SURF is located in a metamorphic uplift zone consisting of multiple interacting anticlines and synclines, resulting in a complex folded structure with intense fracturing (Ulrich et al., 2018). There are three major joint sets as well as a distinct foliation at each of the two sites, including E1-JS1, E1-JS2, E1-JS3, and E1-foliation at E1 site, and E2-JS1, E2-JS2, E2-JS3, and E2-foliation at E2 site. Note that the two sites are distinctly different geological units, so E1-JS1 is different from E2-JS1. As shown in the hemisphere plots of Fig. 1(a), poles to these joint sets represent local averages among clusters of natural fractures that were observed by Ulrich et al. (2018) from mine tunnel surveys and drilled vertical, angled, and horizontal holes (e.g., optical and acoustic televiewer borehole logs).

Fig. 1a also shows the photographs of the specimens that we tested from the two experiment sites. These cylindrical specimens intentionally targeted in-situ natural fractures and were oriented parallel to the natural fractures so that shear could be experimentally induced along the natural fractures. At least one specimen was prepared from each dominant in-situ fracture type, and a description for all specimens is given in Table 2. We tested a variety of features (all under the label "natural fracture" following the terminology of Gale et al. 2014) that included infilled natural fractures (e.g., veins), opening-mode fractures, infilled weak natural fractures, and infilled fractures with locally elevated porosity. For example, two of the specimens, YA02-05 and PS01-11 were separated along the targeted fracture before testing due to weakness. The prior separation for these two specimens prohibited core-plug drilling, so they were prepared as rectangular coupons with a silicone rubber backing to adapt the prepared shape into the cylindrical triaxial direct shear apparatus. YA02-01 was extracted from the amphibolite-rhyolite contact and contained visible pores, so it was also suspected of being weak and permeable.

After the experiments, the infilling minerals of the shear fractures were collected and sent for X-ray powder diffraction analysis (Table 3). These infilling minerals were mainly composed of phyllosilicate, carbonate minerals, tectosilicate, and inosilicate minerals. Relative to the Yates amphibolite and rhyolite, the Poorman schist contained notably higher concentrations of phyllosilicates and graphite. Phyllosilicate and graphite are known to be low-friction materials (Boutareaud et al., 2012; Oohashi et al., 2013). Therefore, they provide a mechanism for reduced frictional strength when present.

2.2 Facility description

The experiments used the triaxial direct-shear method (Fig. 1b to 1e) that was first developed by Carey et al. (2015) and modified by Frash et al. (2016, 2017, 2019a). Here, axial force induces direct-shear stress on targeted fractures by two L-shaped steel pistons. Pore fluid pressure and flow along this fracture are induced by syringe pumps connected to each end of the specimen. Permeability measurements were continuous over the entire experimental procedure. Geomechanical properties of the natural fractures were obtained by aligning the direct-shear load path with natural fractures. A ‘flow path splitter’ in the form of a twisted wire pair was used to avoid fluid channel blockage by small particles or debris generated by shearing the specimen. In-situ x-ray imaging permitted real-time visualization of specimen deformation.

For those specimens whose natural fracture was not along the central plane of the cylindrical specimen (YA02-02, YA02-03, and YA02-04), a 0.2 mm thick segment-disk of stainless-steel sheet metal was inserted to ensure that the initial shear force was applied to only one side of the fracture for measurement of the fracture’s intact strength. For these specimens, shear displacement exceeding ~0.2 mm (i.e., the thickness of the segment-disk) created boundary force changes resulting in fracture of the matrix (Fig. 1e). Post-test inspection of specimens using this method confirmed two end-to-end fractures. In these

experiments, the first shear stress peak gives the strength of the natural fracture, and the second gives the strength of the matrix.

2.3 In-situ stress simulation

In our triaxial direct shear tests, we replicated the principal stress state measured from the E1 and E2 sites (Table 1). For optimal shear orientation, we assumed a 30° angle between the minimum principal stress and the normal to the fracture plane and a 60° angle from the maximum principal stress. None of the sampled fractures or joint sets are optimally oriented for shear, and thus it is unlikely that natural fractures will exactly match this orientation, but this enables the evaluation of hydroshearing potential at the actual site. Using Mohr-Coulomb and Terzaghi's effective stress theory (Eq. 1), this gives the stress parameters shown in Table 1 where the maximum potential in-situ shear stress for the lab tests was estimated at 8.7 MPa for E1 and 7.7 MPa for E2. The corresponding normal total stress was 29 MPa for E1 and 23 MPa for E2. It is important to note that Table 1 includes recent stress measurements from the E1 and E2 sites in addition to the numbers that were used for our laboratory tests. We relied on available data at the time of testing but the differences from recent data are small.

$$\begin{gathered} \sigma_n{}' = \sigma_n - p \ \geq \sigma_T \\ \tau_n \leq \sigma_n' \tan(\varphi) + c \\ \sigma_n = \frac{\sigma_1 + \sigma_3}{2} - \frac{\sigma_1 - \sigma_3}{2} \cos(2\theta) \\ \tau_n = \frac{\sigma_1 - \sigma_3}{2} \sin(2\theta) \end{gathered} \tag{1}$$

In the above, $\sigma_n{}'$ is Terzaghi's effective normal stress, σ_n is normal stress, p is pore pressure, σ_T is the tensile strength, τ_n is shear stress on the fracture, φ is contact friction angle, c is cohesion, σ_1 is maximum principal compressive stress, σ_3 is minimum principal compressive stress, and θ is the angle between the minimum principal stress and the normal to the fracture plane.

Mechanical shear was completed using as much shear stress as needed to induce slip at the applied normal stress. Initial shearing was performed at the in-situ normal stress state for an optimally oriented fracture with respect to hydroshearing potential (Table 2). The use of multiple confining stresses after the first shear event gives a Mohr-Coulomb type failure envelope from the triaxial direct-shear test method.

Based on Eq. (1), the minimum injection pressure (P_{ic}) when hydroshearing could be triggered on an optimally oriented natural fracture can be estimated by the following equation:

$$P_{ic} = 0.5(\sigma_1 + \sigma_3) + \frac{C}{tan(\varphi)} - 0.5(\sigma_1 - \sigma_3)/sin(\varphi) \tag{2}$$

2.4 Experimental procedure

The experiments consisted of shearing the specimens while simultaneously measuring hydro-mechanical properties and fracture geometry. All tests were run at room temperature. Due to the significant differences of each specimen and progressive understanding of their performance, some procedure changes were required. This resulted in the specific procedures for each test varying, but the general procedures are as follows with Fig. 2a as an example:

(1) Set up the specimen as Fig. 1, and increase the confining pressure to the target values, 29 MPa for PS01 specimens and 23 MPa for YA02 specimens. Maintain a pore pressure difference and measure flow rate between the upper and lower ends of the specimen to observe specimen permeability. For example, as shown in Fig. 2a, the inlet pore pressure is 2 MPa, and the outlet pore pressure is 1 MPa.

(2) Apply the direct shear stress at the in-situ stress value, 9.7 MPa for PS01 specimens and 7.7 MPa for YA02 specimens. Attempt hydroshearing by increasing the pore pressure to a value slightly lower than the confining pressure to avoid jacket bursting. If axial displacement increment and/or a shear stress drop were observed during pore pressure increase, it meant that hydroshearing had occurred.

(3) Pore pressure was reduced to original values in Step (1) of 2 MPa inlet pore pressure and 1 MPa outlet pore pressure. Mechanical shearing was performed by increasing the shear stress via axial piston displacement at a steady rate until mechanical failure was observed. This event was indicated by a peak or plateau in shear stress as shear displacement increased.

(4) Optionally, maintain confining pressure and attempt to hydroshear again by increasing the pore pressure. Axial displacement increments and/or a shear stress drop during increasing of pore pressure meant hydroshearing had occurred.

(5) Perform additional mechanical or hydroshearing steps under the same or different confining pressure to measure the hydro-mechanical properties of the fractured specimen. Properties of interest included shear strength and permeability as a function of displacement and measurement of the fracture cohesion and friction angle. The former requires a constant confining stress, while the latter requires changing confining stress.

(6) Cycle the confining pressure to a high and then low value for the measurement of permeability and fracture aperture as a function of confining pressure. This provides a key input of the impact of fracture stiffness for coupled fracture flow and geomechanical models.

(7) Perform dynamic shearing with simultaneous changing of confining pressure and axial displacement to larger displacement magnitudes. This procedure provides information about the shear strength (cohesion and friction angle) and insight into the transient and variable behavior of permeability as a function of

increasing shear damage. This procedure had a high chance of causing confining jacket failure due to dilated apertures often exceeding 2 mm, so this test was reserved for the last stage of testing.

2.5 Permeability calculation

The value of fracture permeability depends on the geometry that is used to define the flow path. In this study, we report the specimen bulk permeability as calculated by (Frash et al., 2017):

$$k = \frac{4Q\mu L}{\pi D^2 \Delta P} \tag{3}$$

Where, Q is volumetric flow rate, μ is dynamic viscosity, L is specimen initial length, D is specimen diameter, and ΔP is the pressure drop across the fracture. Calculating permeability only requires a single flow rate measurement, but we calculate permeability using redundant flow rates from both the inlet and outlet pumps in order to provide an uncertainty estimate (e.g., Fig. 2a). The typical limits of our permeability measurement range are 1 μD to 100 mD.

3 Results and Analysis

Hydro-mechanical measurements were completed for PS01-03, PS01-06, PS01-08, PS01-09, PS01-11, YA02-01, YA02-02, YA02-03, YA02-04, and YA02-05. In-situ x-ray imaging was run for PS01-06 and PS01-11. In our experiments, the dilation (mechanical aperture) was measured using x-ray radiography (Frash et al., 2016, 2019a, b) to measure diameter changes (PS01-06 and PS011-11) or radial linear variable differential transducers (YA02-01, YA02-02, YA02-03, YA02-04, and YA02-05). The error of each method is less than 0.01 mm, which meets our experimental needs. We describe the minimum representative subset of these tests as needed to explain the compiled fracture parameters that we later present. The supplementary information provides additional data for the other tests.

3.1 Naturally fractured Poorman schist (PS01-06)

Fig. 2 shows results from shearing an initially intact, infilled natural-fracture in Poorman schist (E1) specimen PS01-06. This test used x-ray imaging to obtain shear displacement, bulk radial dilation, 3D segmented aperture distribution, specimen rotation, projected 2D fracture void distribution, changes in geometry with time, and location of saturating fluid volumes and the methods were described in Frash et al. (2019a). Sequentially, this experiment included: (1) in-situ x-ray microtomography scan for intact specimen, (2) an intact fracture hydroshearing attempt, (3) mechanical shearing at in-situ confining stress, (4) a second hydroshearing attempt, (5) mechanical shearing at a different effective confining stress via changing pore pressure, (6) stress-dependent permeability, (7) in-situ x-ray microtomography scan for the fractured specimen, and (8) a dynamic shear test. Concurrent radiographs were continuous during the test and provided valuable insights and confirmation of success or failure that conventional measurements are

not able to provide. Full 360° CT scans were obtained before and after the shearing. At the beginning of the test, we can see that the specimen was intact and the natural fracture is invisible to x-rays because it was completely infilled (c.f. Fig. 1a).

The initial hydroshearing attempt involved increasing the inlet pore pressure to 28 MPa, which was limited to be slightly less than the confining pressure of 29 MPa to prevent sleeve failure. However, the infilled fracture permeability was low, so the fluid pressure was unable to promptly diffuse into the fracture. This is an unfavorable condition for hydroshearing at field conditions because pressure must be able to permeate into the natural fracture. Next, we increased the outlet pore pressure to 28 MPa and permitted time for pressure permeation. No shear stress drop, permeability increase, or shear slip was observed, which indicates that hydroshearing did not occur. The x-ray imaging confirmed that no shear stimulation had occurred. After that, mechanical shear was performed, with a direct-shear strength of 58 MPa. A clear shear fracture was generated, connecting both ends of the specimen (Fig. 2d). Specimen permeability increased from less than 10^{-3} mD to the magnitude of 10^{-1} mD. Radial dilation increased from 0.03 mm to 0.14 mm.

With the newly created shear fracture returned to the original in-situ conditions, hydroshearing was attempted again by increasing the inlet pore pressure. With the increased hydraulic conductivity from mechanical shearing, the pore pressure at the outlet now quickly matched the inlet pore pressure. When the pore pressure neared 20 MPa, hydroshearing was confirmed by increased axial displacement, aperture dilation, permeability increase, and shear stress drop. When the specimen was hydrosheared from 0.3 mm to 0.7 mm, the bulk radial dilation increased from 0.14 mm to 0.29 mm (±0.01 mm) and the permeability increased from 10^{-1} mD to a maximum of 10 mD. The corresponding x-ray radiographs (Fig. 2d to Fig. 2e) show increasing damage from hydroshearing. After shearing, the fracture permeability retained a 25-fold permeability enhancement (1 mD compared with 0.04 mD). The retained permeability is similar to prior findings (Ye and Ghassemi 2018, Kluge et al., 2020) and confirms the ability of hydroshearing to stimulate permeable fractures in the Poorman schist.

After hydroshearing, we further mechanically sheared the specimen at different effective confining stresses. This provides a measure of residual fracture cohesion and internal friction angle. Finally, the stress-dependent properties (e.g., permeability) were measured, and dynamic shear was performed. Dynamic shear provides another measurement for the relationship between shear stress and confining pressure, and these values closely agreed with the stepwise measurement, as to be described in later sections.

Observations of this type were used to modify the experiment procedures for follow-on tests to better target many different parameters of interest. Our ultimate goal here was to identify natural fractures that were capable of hydroshearing at the EGS Collab E1 and E2 while also obtaining measurements of the fracture properties that are needed for future multiphysics predictive models.

3.2 Mechanical properties of shear fractures

All fractures were sheared under multiple confining pressures and key values are summarized in Table 4. Additional details regarding each test are provided in the Supporting Information. Using our results, we optimized Mohr-Coulomb type failure curves to determine fracture cohesion and friction angle (Fig. 3). Combined these results with in situ stresses into Eq. (2), the theoretical pore pressure to cause hydroshearing can be calculated (Table 4).

Other than the weakest specimens PS01-11 and YA02-05, the tested natural fractures from E1 and E2 were too strong for hydroshearing at normal and shear stresses for optimally oriented fractures. For the exceptionally weak fracture of PS01-11, only 6 MPa of fluid pressure was theoretically needed to induce hydroshearing. In this test, hydroshearing occurred when the pore pressure reached 7.4 MPa (Table 4). While slightly stronger, the weak YA02-05 specimen was hydrosheared at a critical pore pressure of 17.8 MPa, slightly larger than the theoretical predicted value of 16.7 (±0.7) MPa. In contrast, a pore pressure of 49 MPa was theoretically needed to hydroshear the PS01-09 specimen, so the actual hydroshearing could not occur due to the limitation of our experimental confining pressure of 29 MPa. Overall, most of the infilled natural fractures were too strong for hydroshearing. For these strong fractures, the critical pressure for hydroshearing was higher than that for hydraulic fracturing. The cohesion we measured for these infilled fractures was between 3.24 and 13.4 MPa, and friction angle was between 24.1 to 41.8° (friction coefficient between 0.45 to 0.89).

3.3 Shear effect on apparent frictional coefficient

The apparent friction coefficient (μ_a) of fractures is defined as the ratio of shear stress (τ) to effective confining pressure (σ_n'). Fig. 4 shows the apparent friction coefficient for all tested specimens during hydroshearing and mechanical shear. Since the fracture is rough with cohesion, the 'apparent frictional coefficient' calculated here is higher than the actual 'friction coefficient' of the fracture achieved from Mohr-Coulomb type failure curves shown in Table 4 and Fig. 3. The key point here is to discuss how the fracture shear strength changes under the same effective normal stress during shearing.

Hydroshearing can reduce the apparent frictional coefficient of fractures. The coefficient values were calculated by mechanical shearing data under the same effective normal stress prior and after the hydroshearing. For example, Fig. 4(a) shows that the apparent frictional coefficient of PS01-06 drops from (1.04-1.1) to (0.63-0.85) after hydroshearing, and Fig. 4(b) and Fig. 4(c) also show that the apparent frictional coefficient dropped after hydroshearing for PS01-08 (from 1.23 to 1.20) and YA02-05 (from 1.10 to 1.06). During hydroshearing, the pore fluids dilate the fractures and decrease effective normal stresses. This helps to reduce asperity damage, decrease the effect of small-scale asperity interlocking, and

effectively lubricate fractures. Later, when pore pressure returns to the original low level, the fracture dilation reduced but part of the dilation was maintained (In Figure S2, the dilation of PS01-08 increased from 2.9 mm to 3.4 mm, and retained to 3.0 mm after hydroshearing). The fracture surface was self-propped and unable to regain the strong interlocking performance antecedent to hydroshearing.

Mechanical shearing can also reduce the apparent frictional coefficient of an existing fracture (Fig. 4d), but with a different mechanism compared to hydroshearing. This could be attributed to the comminution of asperities and gouge for reduced effective surface roughness (Attache and Mellas 2017). Post-test inspection of the specimens confirmed fine particle generation inside of the shear fractures (Fig. S12). Compared to mechanical shearing under high normal stress, it appears that hydroshearing could be linked to strain-weakening behavior and increased conductivity.

3.4 Permeability enhancement and mineral compositions

The change of permeability after shearing is summarized in Table 4. As shown in Table 4, the intact permeability of the natural fractures was less than our 10^{-3} mD measurement limit, except for the pre-separated weak foliation PS01-11 and the pre-separated rhyolite fracture YA02-05. Hydroshearing during stimulation would be difficult or impossible for the low hydraulic conductivity fractures. After mechanical shear, the fractured specimens exhibited permeability greater than 0.01 mD (more than 10 times greater than original values), with the exception of the white mineral infilled amphibolite (YA02-03). For those specimens with the occurrence of hydroshearing, the fracture permeability generally increased to 10 times greater than values before hydroshearing. The only exception is the pre-fractured weak foliation PS01-11 specimen where, instead of enhancing the permeability, the hydroshearing decreased the fracture permeability.

The hydraulic and mechanical properties of fractures can be linked to their mineralogical composition and properties (Davatzes et al., 2010; Cavailhes et al., 2013). Through XRD analysis of fracture materials in Table 3, we found that reduced shear strength and permeability reduction during shear were correlated with higher phyllosilicate (sheet mineral) content. For example, the high content of phyllosilicates (77.3%) in the weak PS01-11 fracture associates with shear compaction and permeability loss when sheared. This mineralogy was distinct relative to all of the other specimens that contained significantly less phyllosilicates. Phyllosilicates are strongly anisotropic layered and weak minerals. Shear can cause rotation, delamination, ripplocation, and grain cracking of phyllosilicate minerals, resulting in more gouge production (Sánchez-Roa et al., 2017; Aslin et al., 2019). Precipitates could also be generated through reactions between phyllosilicate minerals and pore fluid (Behnsen and Faulkner, 2011). Thus, we suggest that the reduced strength and permeability in PS01-11 originated from shear-produced gouge powders potentially containing

chemical precipitates. This is consistent with prior work that observed fracture permeability decreases with phyllosilicate content and increases with tectosilicate content for shale, and observations of a lower frictional strength for phyllosilicate rich rocks (Fang et al., 2018a; An et al., 2020).

3.5 Mechanical and hydraulic apertures at a different effective confining pressure

The mechanical and hydraulic aperture relationship has been studied extensively for unconventional shale rocks (Frash, 2016, 2019c; Li et al., 2021). Mechanical aperture is a measure of the porous aperture (i.e., void) of a fracture and the hydraulic aperture is a measure of fracture fluid flow potential (comparable to permeability or hydraulic transmissivity). Due to fracture surface roughness, hydraulic aperture, that determines fracture permeability, often deviates significantly from mechanical aperture. Here, we explore the response of both mechanical and hydraulic fracture aperture to shear and changing effective stress in crystalline rocks to provide key inputs for field-scale multiphysics simulations of geothermal energy extraction.

In our experiments, the net mechanical aperture was measured by specimen dilation using either x-ray radiography (Frash et al., 2016, 2019a) to measure 2D external surface displacement (PS01-06 and PS011-11) or a radial linear variable differential transducer (YA02-01, YA02-02, YA02-03, YA02-04, and YA02-05). The hydraulic aperture was calculated from the pressure and flow rate measurements based on an equivalent smooth parallel plate model (Witherspoon et al., 1980):

$$b_h = \sqrt[3]{\frac{12\mu LQ}{\Delta P D}} \tag{4}$$

where b_h is the fracture effective hydraulic aperture, μ is the fluid dynamic viscosity, L is the specimen length, Q is the volumetric flow rate, D is the specimen diameter (i.e., fracture width), ΔP is the fluid pressure drop between the inlet and outlet ends of the specimen.

Generally, the hydraulic aperture is lower than the mechanical aperture because of the existence of contact areas within the fractures, fracture roughness and tortuosity (Xiong et al., 2011). Both mechanical aperture and hydraulic aperture are important for fluid flow, with the former controlling porosity and the latter controlling flow rates (Li et al., 2021). However, mechanical aperture and hydraulic aperture are influenced by effective normal stress (Wu et al., 2017; Fang et al., 2018b). To interrelate these parameters, we first determine mechanical aperture as a function of effective confining pressure (Barton et al., 1985) and then we relate mechanical aperture to the hydraulic aperture calculated by fluid flow measurements (Witherspoon et al., 1980). Here, we consider two models for the relationship between the mechanical aperture and effective confining pressure: the Barton et al. (1985) model and an exponential decay model (Li et al., 2021).

Barton et al. model (1985):

$$b_d = b_{b0} - \frac{A\sigma_n'}{1 + B\sigma_n'} \quad (5)$$

where, σ_n' is the effective normal stress; b_{b0} is the initial mechanical aperture, which represents the mechanical aperture with zero effective normal stress; b_d is the mechanical aperture at a certain effective normal stress; A and B are fitted constants.

Exponential model:

$$b_d = b_{e0} e^{-\alpha \sigma_n'} \quad (6)$$

where b_{e0} is the initial mechanical aperture, which represents the mechanical aperture with zero effective normal stress, and α is the fitted compressibility coefficient.

After finding the mechanical aperture, we determine the relationship between mechanical and hydraulic apertures (N) using the following relationship:

$$b_h^{fitted} = N b_d^{measured} \quad (7)$$

$$\chi^2 = \Sigma (b_h^{fitted} - b_h^{measured})^2 \quad (8)$$

where N is the ratio between hydraulic aperture and mechanical aperture, which we call a 'modified Witherspoon factor', paying tribute to the pioneering work by Witherspoon et al. (1980). By minimizing the error term χ^2, we obtain the optimized Witherspoon factor N in a form that is suited for relating mechanical aperture to hydraulic aperture in models.

Fig. 5 and Table 5 provide the fitted results for the above models. We prefer the exponential model for our subsequent estimation of the modified Witherspoon factor because that model is scalable and doesn't suffer from predictions of "negative" apertures at high stress. Based on the fitted mechanical aperture from the exponential model, we fit the modified Witherspoon factor to the measured mechanical and hydraulic apertures. Renshaw (1995) points out that the ratio between mechanical and hydraulic aperture depends on fracture surface roughness. The compressibility of our crystalline rock specimens in our exponential aperture model ranges between 0.0076 and 0.0145 MPa^{-1}. For more ductile shale rocks, values higher than 0.089 MPa^{-1} have been observed. The fracture compressibility value was shown to have significant influence on cumulative hydrocarbon energy production (Li et al., 2021).

Hydraulic and mechanical aperture both decrease with increasing confining pressure, but the fractures maintain an aperture even at very high confining pressure. We also find that the mechanical aperture is dependent on the stress history (loading vs. unloading), but the hydraulic aperture dependence on stress history is less obvious. Similarly, Witherspoon et al. (1980) and Kluge et al. (2020) found pressure cycling

led to reversible permeability changes, whereas Ye and Ghassemi (2018) found the permeability change is irreversible. This appears to indicate a dependency of stress-dependent aperture behavior on material properties and surface roughness. If the stress history caused degradation of fracture asperities, the permeability is more likely to be irreversible (Vogler et al., 2016).

A key observation from these results is that b_h/b_d ratios can be orders of magnitude smaller than 1. The prior publications that used saw-cut fractures as opposed to natural fractures were unable to see this result (Witherspoon et al., 1980; Zimmerman and Bodvarsson et al., 1996; Nemoto et al., 2008), so these earlier works report b_h/b_d ratios closer to 1. This finding highlights the need to consider actual fracture properties, inclusive of roughness effects, in order to accurately model fracture-dominated subsurface flow and transport. Overall, the stress change causes mechanical deformation of the fracture, and fracture permeability can be estimated by using the measured quantitative relationships of stress dependent mechanical apertures and stress dependent hydraulic apertures. Moreover, the measured values and variations of hydraulic aperture, mechanical aperture, and modified Witherspoon factor can be used in post-stimulation modeling and explain how the uncertainties can change the flow behavior at the reservoir scale. The stress-induced fracture closure has been proved to cause a significant loss of cumulative shale gas production in certain scenarios (Li et al., 2021). Similar deformation-diffusion coupled mechanisms could exist for geothermal energy as well (Pandey et al., 2018; Anyim and Gan, 2020) and need further investigation.

4 Application to EGS Collab Experiment 1 and 2 Sites

To evaluate our results and apply them to inform field decision making, we must first employ slip tendency analysis. Using this analysis, we can optimize well orientations with respect to natural fractures that are suited for hydroshearing. As mentioned in the Introduction, the EGS Collab Project aims to investigate how hydraulic stimulation experiments (hydraulic fracturing and hydroshearing) could enhance fluid flow in fracture-dominated high-stress crystalline-rock. At the EGS Collab Experiment 1 site (E1), the goal was to study hydraulic fracturing as a means to stimulate flow from an injection well to a production well. Conversely, at the E2 site, the goal is to encourage hydroshearing as much as possible. Stochastic analysis that considers fracture positional data (e.g., well logs), in-situ stress data (e.g., hydrofrac tests; Ingraham et al., 2020), well placement options (e.g., drift geometry limitations), and fracture strength and permeability data (e.g., triaxial direct-shear measurements) can be used to improve site design. Here we demonstrate such an analysis, but for brevity we exclude details that can be found in Singh et al. (2019) and other related publications from the EGS Collab Project. To aid others with similar efforts, we note that an open-source software package named the “Fat Crayon Toolkit” was developed to complete the EGS Collab Team’s analysis and is now available for use (Morris, 2021). The analysis presented here will show how triaxial

direct-shear measurements can aid well design based on our experience with EGS Collab E1 and E2. The relevant field site plots are shown as Fig. S14 in the Supplement Information.

4.1 Improved slip tendency analysis

Conventional slip tendency analysis can be used to identify joint set orientations that are subjected to shear stress and to quantify how weak those fractures must be to hydroshear. To interpret conventional slip tendency analysis, a global fracture cohesion of 0.0 MPa and a friction coefficient of 0.6 is typically assumed when site-specific data is unavailable (Byerlee, 1978; Singh et al., 2019). Here, we perform this analysis in the context of the minimum injection pressure that is required to induce shear slip or tensile opening (Fig. 6a and Fig. 6b). This enables both shear and tensile failure mechanisms to be included in the same plot. Using measurements of the in-situ stress state and joint set orientations (Table 1) for E1 and E2, we can start our analysis by identifying all the natural fractures that are suitably oriented for shear using Eq. (1). The conventional slip tendency analysis predicts that E1-JS1 is likely best oriented for shear at the Experiment 1 site, and E2-JS2 and E2-JS3 are oriented for shear at the Experiment 2 site.

We can increase the relevance of our predictions to injection-induced slip by additionally considering the triaxial direct-shear measured permeability and strength of the fractures belonging to each joint set. Based on the general knowledge that fractures follow the path of least resistance, we can expect that the weakest fractures that are also permeable will be activated first in response to fluid injection. Furthermore, the activation of these weak fractures can preclude the activation of stronger fractures due to the inability of the rock-mass to attain higher-stress states caused by stress relief and the reduction in fluid pressure owning to fluid losses into the previously activated fractures. Therefore, we can focus on the minimum injection pressure required to induce shear slip or tensile opening using the properties of the weakest site-specific fractures (Fig. 6c and Fig. 6d). Also, we can omit any fractures having intact permeability of less than 10^{-3} mD since they will be effectively impermeable with respect to the typical duration of a hydraulic stimulation treatment at 48 hours or less. From all the above analysis, we found the best candidate fractures for hydraulic shearing are: E1-JS4 and foliation that steeply dips to the southwest at the Experiment 1 site; and Joint Set 3 (JS3) and foliation at the Experiment 2 site. The permeability requirement eliminates E1-JS1 at the E1 site and E2-JS2 at the E2 site as good candidates for hydroshearing.

4.2 Field validation of shearing at the E1 site

As previously stated, the goal at E1 was to stimulate hydraulic fractures. Following hydraulic fracturing convention, our drilling plan followed the common practice of drilling the injection and production wells parallel to the minimum principal stress, which at E1 was to the north and slightly dipping downwards. Owing to intense natural fracturing in and around the E1 site, we were aware of the potential for natural

fracture shear stimulation and that one prominent foliation-parallel permeable natural fracture (also called "OT-P connector" by Fu et al., 2021) was close to the injection well. However, this natural fracture was not considered in the hydraulic fracturing design. In hindsight, our analysis and the site data predicted that hydroshearing was likely to occur at this site at pressures lower than the hydraulic fracture limit, especially along this foliation-parallel natural fracture (Fig. 6c). When E1 was hydraulically stimulated, field data provided clear evidence that the fluid injection stimulated new hydraulic fractures and also produced flow through this prominent foliation-parallel natural fracture. This data set included microseismic mapping, tracer circulation tests, and direct visual observations of flow into the production well (Fu et al., 2021). The field observation of this permeable fractures parallel to foliation is consistent with our laboratory based predictions that foliation-parallel fractures are the most likely to be permeable.

However, it is important to note that the field data set is unable to fully confirm that hydroshearing occurred along this foliation-parallel fracture due to the absence of microseismicity along this fracture and the absence of displacement measurements across this fracture. If we acknowledge that shear slip can be aseismic, the absence of microseismic data does not imply an absence of shear displacement. Therefore, while we cannot confirm that hydroshearing occurred, we can at least claim that this natural fracture (OT-P connector) aligned with a known weak, permeable, and shear-oriented joint set (Joint Set 4 and foliation-parallel orientation). In addition, we can confirm that fluid did flow through this fracture during stimulation and fluid circulation tests. Also, knowing that naturally occurring shear is a common mechanism for permeability along existing fractures, we can anticipate that shear was likely the cause of the high permeability of this foliation-parallel fracture, whether or not the shear occurred before or during the fluid injection. In summary, the field data, triaxial direct-shear measurements, and the slip tendency analysis all agree that the foliation-parallel fractures at the E1 site are good candidates for hydroshearing, thus validating our analysis.

4.3 Selection of E2 well orientations

At the ongoing E2 site development, our analysis provides *a priori* predictions. Instead of hydraulic fracturing, this new experiment is targeting hydroshearing as the mechanism to stimulate flow between injection and production wells. The high strength of the measured natural fractures indicates that hydroshearing will be more challenging at the E2 site than it was at the E1 site, e.g., YA02-05 is stronger than PS01-11. We still benefit from the improved slip-tendency analysis that identified E2-JS3 and foliation as the top candidates for hydraulic shear stimulation at E2 to intercept a maximum number of natural fractures that are poised for shear slip. If intercepting natural fracture hydroshearing targets was the sole design consideration, a well parallel to the indicated hydroshearing vector (i.e., E2-JS3 and foliation; Fig. 6d) would have been the ideal choice. However, due to field constraints and equipment limitations, drilling

in the optimal orientation was not feasible, which led to the decision to drill northeast oriented wells at a shallow dip (Fig. 6f). This orientation will miss some of the shear critical fractures but is suited for intersecting fractures from E2-JS3 and it is coincident with the peak of in-situ shear stress. Future work will reveal the effectiveness of this ultimate selection, but our experience from E1 and the slip tendency analysis for E2 supports this choice of well orientation for high potential for inducing hydroshearing. Without the benefit of the improved slip tendency analysis, previous designs that targeted E2-JS2 (e.g., 260° AzN and 69° dip; Frash and Morris, 2019d) were incorrectly thought to have been preferable.

5 Discussion

As we demonstrated here, triaxial direct-shear measurements, or similar methods to characterize natural fracture strength, stiffness and permeability, can be used to improve site design and diagnostics. A maximum benefit is obtained when the analysis uses site-specific core and then targets suspected weak fractures or weak rock fabric, especially when the sample set is limited in number. Identifying observable fractures that are weak and permeable is not self-evident from well logs (Fig. S15), so tests such as our triaxial direct-shear are needed to provide insight to better inform target selection.

Commercial EGS requires stimulating rock in such a way that high flow rates can be sustained at low injection pressures. Gischig and Preisig (2015) estimate that a permeability of at least 0.01 to 1 mD could be adequate economically. Our laboratory results indicate that the EGS Collab sites can achieve this level of enhancement through hydroshear stimulation. However, the E1 field site used hydraulic fractures (not shear) to inject fluid into the rock. This was observed to require continuous injection at 30 MPa for both hydraulic fracturing stimulation and for long-term circulation tests. In this case, the fractures connecting to the injection well were propped open by the injection pressure, not by proppant or shear dilation (Kneafsey et al., 2019). Continuous injection at hydrofracture pressures is a challenge when upscaled to commercial EGS due to the technical demands of high-pressure pumping. Adding proppants is unlikely to solve this problem because most commercial proppants are known to perform poorly at high-pressure, high-temperature conditions (Liang et al., 2016). This result emphasizes the importance and attraction of shear stimulation to sustain flow at low pressures. If an EGS system is to be designed using hydroshearing for the primary stimulation method, identifying fractures that are suitable for hydroshearing will be crucial. However, our hydro-mechanical measurements show that it would be a mistake to assume that an observable fracture at a shear-prone orientation implies a weak or permeable fracture. Whether fractures are weak or permeable can be difficult to be observed from image logs. Fig. S15 shows that YA02-05 can be reasonably interpreted as an infilled fracture and PS01-11 is almost invisible in the image logs. Instead, well pumping tests or shear tests are necessary to confirm shear slip potential for the natural fractures.

Furthermore, analysis using measurements such as what we presented benefits from acknowledging uncertainty in the subsurface. This includes the possibility of stronger or weaker fractures than what is measured as well as less or more permeable fractures. Furthermore, a comprehensive analysis would benefit from considering that single fractures can be very rough and multi-stranded which has a tendency to significantly reduce the effective hydraulic aperture to mechanical aperture ratio (b_d/b_h). For the sake of public awareness, the "Fat Crayon Toolkit" and similar stochastic tools (Morris, 2021; Frash, 2021) offer a start to addressing this need by considering uncertainty early in the design process. In practice, it is challenging to consider these details and their uncertainty in the design process when time is limited and decisions must be made before all of the data is available. Future work that focuses on accelerating the use of measurements to reduce uncertainty would help inform design decisions and achieve higher performing geothermal energy systems.

6 Conclusions

In our study, we completed hydro-mechanical measurements on crystalline rock specimens from the EGS Collab field sites E1 and E2. The characterized fracture properties include permeability enhancement by shearing, fracture mineral compositions, fracture and rock matrix strengths, mechanical and hydraulic apertures at different confining stress, and frictional strength. From this work, several conclusions were drawn:

(1) Triaxial direct-shear measured permeability and fracture strength can be used to improve predictions for hydroshearing. We demonstrated that pre-existing natural fractures must be mechanically weak, favorably oriented, and sufficiently permeable to be hydrosheared. Through improved slip tendency analysis using fracture orientation data, in-situ stress data, fracture strength and permeability data, we identified that the E1-JS4 and foliation in E1 site and E2-JS3 and foliation in E2 site are top candidates for hydroshearing.

(2) Our in situ generated rough-surfaced crystalline fractures exhibited 1 to 3 orders of magnitude decoupling between mechanical aperture and hydraulic aperture, cohesion of 1.9 to 20 MPa (mostly less than 6.8 MPa), frictional angle of 17 to 41.8°, and compressibility in our exponential aperture model of 0.0076 and 0.0145 MPa^{-1}. This provides key inputs for future field-scale multiphysics simulations of energy extraction.

(3) After shearing, the fracture permeability increased and was retainable in most cases, often from less than 10^{-3} mD to higher than 0.01 mD. However, one specimen (PS01-11) that was phyllosilicate rich exhibited shear compaction and permeability reduction after shearing. Therefore, it should not be assumed that shear stimulation will always result in higher hydraulic conductivity.

(4) Overall, our measurements provided useful data for EGS Collab design decisions and diagnostics by identifying natural fracture sets that were most suitable for hydroshearing. If applied at other sites, targeted triaxial direct-shear tests combined with in-situ stress measurements could provide valuable constraints for predicting the effects of hydraulic stimulation in fracture-dominated rock systems.

Acknowledgements and Data Availability

Funding: This work is supported by Department of Energy (DOE) Basic Energy Sciences under FWP LANLE3W1. The EGS Collab work in this study is supported by the U.S. Department of Energy, Office of Energy Efficiency and Renewable Energy (EERE), Geothermal Technologies Office (GTO) under Contract No. 89233218CNA000001 with Los Alamos National Laboratory, led by Contract No. DEAC02-05CH11231 with Lawrence Berkeley National Laboratory. Research supporting this work took place in whole or in part at the Sanford Underground Research Facility in Lead, South Dakota. The assistance of the Sanford Underground Research Facility and its personnel in providing physical access and general logistical and technical support is gratefully acknowledged.

Author contributions: Laboratory experiments were conducted and analyzed by L.P.F., J.C.H., and N.J.W. Data from the EGS Collab site was collected by the EGS Collab team with the values in this manuscript extracted by L.P.F., G.N., and P.F. Numerical modelling with GEOS was performed by P.F. and J.M. Projects making this work possible were led by M.G., J.W.C., and T.K.

Competing interests: All authors declare no conflicts of interest.

Data and materials availability: Data for the Hijiori Hot Dry Rock project seismic events was provided by Yanagisawa, N. The EGS Collab project is ongoing with data available on the Geothermal Data Repository (GDR).

EGS Collab Team: J. Ajo-Franklin[LBNL,Rice], T. Baumgartner[SURF], K. Beckers[NREL], D. Blankenship[SNL], A. Bonneville[PNNL], L. Boyd[DOE], S. Brown[NETL], J.A. Burghardt[PNNL], C. Chai[ORNL], A. Chakravarty[LBNL], T. Chen[LANL], Y. Chen[LANL], B. Chi[Rice], K. Condon[UWM], P.J. Cook[LBNL], D. Crandall[NETL], P.F. Dobson[LBNL], T. Doe[TDG], C.A. Doughty[LBNL], D. Elsworth[Penn], J. Feldman[SNL], Z. Feng[LANL], A. Foris[SNL], L.P. Frash[LANL], Z. Frone[DOE], P. Fu[LLNL], K. Gao[LANL], A. Ghassemi[OU], Y. Guglielmi[LBNL], B. Haimson[UWM], A. Hawkins[Stanford], J. Heise[SURF], C. Hopp[LBNL], M. Horn[SURF], R.N. Horne[Stanford], J. Horner[PNNL], M. Hu[LBNL], H. Huang[former INL], L. Huang[LANL], K.J. Im[Penn], M. Ingraham[SNL], E. Jafarov[LANL], R.S. Jayne[LBNL], T.C. Johnson[PNNL], S.E. Johnson[LBNL], B. Johnston[NREL], S. Karra[LANL], K. Kim[LBNL], D.K. King[SNL], T. Kneafsey[LBNL], H. Knox[PNNL], J. Knox[PNNL], D. Kumar[OU], K. Kutun[CSM], M. Lee[SNL], D. Li[LANL], J. Li[LANL], K. Li[Stanford], Z. Li[Penn], M. Maceira[ORNL], P. Mackey[NETL], N. Makedonska[LANL], C.J. Marone[Penn], E. Mattson[MH], M.W. McClure[RF], J. McLennan[UU], T.

McLing[INL], C. Medler[SDSMT], R.J. Mellors[LLNL], E. Metcalfe[DOE], J. Miskimins[CSM], J. Moore[NETL], C.E. Morency[LLNL], J.P. Morris[LLNL], T. Myers[SNL], S. Nakagawa[LBNL], G. Neupane[INL], G. Newman[LBNL], A. Nieto[DOE], T. Paronish[NETL], R. Pawar[LANL], P. Petrov[LBNL], B. Pietzyk[SURF], R. Podgorney[INL], Y. Polsky[ORNL], J. Pope[SNL], S. Porse[DOE], J.C. Primo[LBNL], C. Reimers[SDSMT], B.Q. Roberts[PNNL], M. Robertson[LBNL], V. Rodriguez-Tribaldos[LBNL], W. Roggenthen[SDSMT], J. Rutqvist[LBNL], D. Rynders[SURF], M. Schoenball[NAGRA], P. Schwering[SNL], V. Sesetty[OU], C.S. Sherman[LLNL], A. Singh[Stanford], M.M. Smith[LLNL], H. Sone[UWM], E.L. Sonnenthal[LBNL], F.A. Soom[LBNL], D.P. Sprinkle[PNNL], S. Sprinkle[LBNL], C.E. Strickland[PNNL], J. Su[SNL], D. Templeton[LLNL], J.N. Thomle[PNNL], C. Ulrich[LBNL], N. Uzunlar[SDSMT], A. Vachaparampil[OU], C.A. Valladao[LBNL], W. Vandermeer[DOE], G. Vandine[SURF], D. Vardiman[SURF], V.R. Vermeul[PNNL], J.L. Wagoner[LLNL], H.F. Wang[UWM], J. Weers[NREL], N. Welch[LANL], J. White, M.D. White[PNNL], P. Winterfeld[CSM], T. Wood[LBNL], S. Workman[NETL], H. Wu[LLNL], Y.S. Wu[CSM], E.C. Yildirim[Penn], Y. Zhang[Stanford], Y.Q. Zhang[LBNL], Q. Zhou[LBNL], M.D. Zoback[Stanford]

References

Acosta, M., Maye, R., & Violay, M. (2020). Hydraulic transport through calcite bearing faults with customized roughness: effects of normal and shear loading. *Journal of Geophysical Research: Solid Earth*, 125(8), e2020JB019767.

An, M., Zhang, F., Elsworth, D., Xu, Z., Chen, Z., & Zhang, L. (2020). Friction of Longmaxi shale gouges and implications for seismicity during hydraulic fracturing. *Journal of Geophysical Research: Solid Earth*, 125(8), e2020JB019885.

Anyim, K., & Gan, Q. (2020). Fault zone exploitation in geothermal reservoirs: production optimization, permeability evolution and induced seismicity. *Advances in Geo-Energy Research*. 4(1): 1-12.

Aslin, J., Mariani, E., Dawson, K., & Barsoum, M. W. (2019). Ripplocations provide a new mechanism for the deformation of phyllosilicates in the lithosphere. *Nature communications*, 10(1): 1-9.

Bauer, S. J., Huang, K., Chen, Q., Ghassemi, A., & Barrow, P. C. (2016). Experimental and Numerical Investigation of Hydro-Thermally Induced Shear Stimulation. Paper presented at the 50th U.S. Rock Mechanics/Geomechanics Symposium, Houston, United States.

Boutareaud, Sébastien, Takehiro Hirose, Muriel Andréani, Matej Pec, Dan-Gabriel Calugaru, Anne-Marie Boullier, & Mai-Linh Doan. 2012. On the role of phyllosilicates on fault lubrication: Insight from micro-and nanostructural investigations on talc friction experiments. *Journal of Geophysical Research: Solid Earth* 117(B8).

Brinton, D. (2011). Issues surrounding fracturing of geothermal systems – predicting thermal conductivity of reservoir rocks and evaluating performance of fracture proppants, (MS Thesis). Salt Lake City: University of Utah.

Bromley, C. J., Mongillo, M., Hiriart, G., et al. (2010). Contribution of geothermal energy to climate change mitigation: the IPCC renewable energy report. Paper presented at Proceedings World Geothermal Congress 2010, Bali, Indonesia.

Byerlee, J. 1978. Friction of rocks. *Pure and Applied Geophysics:* 116: 615-626.

Carey, J. W., Lei, Z., Rougier, E., Mori, H., and Viswanathan, H. S. (2015). Fracture- permeability behavior of shale. Journal of Unconventional Oil and Gas Resources, 11:27–43. doi: 10.1016/j.juogr.2015.04.003.

Cavailhes, T., Soliva, R., Labaume, P., Wibberley, C., Sizun, J. P., Gout, C., Charpentier D., Chauvet A., Scalabrino B., & Buatier, M. (2013). Phyllosilicates formation in faults rocks: Implications for dormant fault-sealing potential and fault strength in the upper crust. *Geophysical Research Letters*, 40(16): 4272-4278.

Chen, Z., Narayan, S. P., Yang, Z., & Rahman, S. S. (2000). An experimental investigation of hydraulic behaviour of fractures and joints in granitic rock. *International Journal of Rock Mechanics and Mining Sciences*, 37(7): 1061-1071.

Davatzes, N.C. and S. H. Hickman. (2010). The Feedback Between Stress, Faulting, and Fluid Flow: Lessons from the Coso Geothermal Field, CA, USA. Paper presented at proceedings World Geothermal Congress 2010, Bali, Indonesia.

Dezayes, C., Genter, A., & Valley, B. (2010). Structure of the low permeable naturally fractured geothermal reservoir at Soultz. *Comptes Rendus Geoscience*, 342(7-8): 517-530.

Dobson, P., Kneafsey, T. J., Blankenship, et al. (2017). An introduction to the EGS Collab Project. *GRC Transactions*, 41: 837-849.

Esaki, T., Du, S., Mitani, Y., Ikusada, K., and Jing, L. (1999). Development of a shear-flow test apparatus and determination of coupled properties for a single rock joint. International Journal of Rock Mechanics and Mining Sciences, 36(5): 641-650.

Fan, Melissa. (2020). Digging Deeper into Enhanced Geothermal Systems: Techno-Economic Simulation of EGS Electricity Generation Development. (Thesis). Princeton: Princeton University.

Fang, Y., Elsworth, D., Wang, C., & Jia, Y. (2018a). Mineralogical controls on frictional strength, stability, and shear permeability evolution of fractures. *Journal of Geophysical Research: Solid Earth*, 123(5): 3549-3563.

Fang, Y., Elsworth, D., Ishibashi, T., & Zhang, F. (2018b). Permeability evolution and frictional stability of fabricated fractures with specified roughness. *Journal of Geophysical Research: Solid Earth*, 123(11): 9355-9375.

Frash, L. P., Carey, J. W., Lei, Z., Rougier, E., Ickes, T., & Viswanathan, H. S. (2016). High-stress triaxial direct-shear fracturing of Utica shale and in situ X-ray microtomography with permeability measurement. *Journal of Geophysical Research: Solid Earth*, 121(7): 5493-5508.

Frash, L. P., Carey, J. W., Ickes, T., & Viswanathan, H. (2017). Caprock integrity susceptibility to permeable fracture creation. *International Journal of Greenhouse Gas Control*, 64: 60-72.

Frash, L. P., Carey, J. W., & Welch, N. J. (2019a). Scalable En Echelon Shear-Fracture Aperture-Roughness Mechanism: Theory, Validation, and Implications. *Journal of Geophysical Research: Solid Earth*, 124(1): 957-977.

Frash, L. P., Carey, J. W., Welch, N. J., & EGS Collab Team. 2019b. EGS Collab Experiment 1 Geomechanical and Hydrological Properties by Triaxial Direct Shear. Paper presented at 44th Workshop on Geothermal Reservoir Engineering. California, United States.

Frash, L. P., Welch, N. J., Carey, J. W., & EGS Collab Team. 2019c. Geomechanical evaluation of natural shear fractures in the EGS Collab Experiment 1 test bed. Paper presented at the 53rd U.S. Rock Mechanics/Geomechanics Symposium, New York City, United States.

Frash, L.P. and Morris, J.P. (2019d) Stochastic prediction of multi-well fracture connectivity and application to EGS Collab Experiment 2. Paper presented at the proceedings of the 53rd US Rock Mechanics / Geomechanics Symposium, New York, June 23-26.

699 Fu, P., Schoenball, M., Ajo-Franklin, J.B., Chai, C., et al. (2021) Close observation of hydraulic
700 fracturing at EGS Collab Experiment 1: fracture trajectory, microseismic interpretations,
701 and the role of natural fractures. *Journal of Geophysical Research - Solid Earth.*
702 Gale, Julia FW, Stephen E. Laubach, Jon E. Olson, Peter Eichhubl, and András Fall. (2014).
703 Natural fractures in shale: A review and new observations: Natural Fractures in Shale: A
704 Review and New Observations. *AAPG bulletin*, 98(11): 2165-2216.
705 Gentier, S., E. Lamontagne, G. Archambault, & J. Riss (1997), Anisotropy of flow in a fracture
706 undergoing shear and its relationship to the direction of shearing and injection pressure,
707 *International Journal of Rock Mechanics and Mining Sciences*, 34(3-4): 94.e1-94.e12.
708 Gischig, V. S., & Preisig, G. (2015). Hydro-fracturing versus hydro-shearing: a critical assessment
709 of two distinct reservoir stimulation mechanisms. Paper presented at 13th ISRM
710 International Congress of Rock Mechanics. Montreal, Canada.
711 Hamm, S. (2019). GeoVision: Harnessing the heat beneath our feet. U.S. Department of Energy.
712 Hincks, T., Aspinall, W., Cooke, R., & Gernon, T. (2018). Oklahoma's induced seismicity strongly
713 linked to wastewater injection depth. *Science*, 359(6381): 1251-1255.
714 Im, K., Elsworth, D., & Fang, Y. (2018). The influence of preslip sealing on the permeability
715 evolution of fractures and faults. *Geophysical Research Letters*, 45(1): 166-175.
716 Ingraham, M.D., Schwering, P.C., Burghardt, J., Ulrich, C., Doe, T., Roggenthen, W.M., Reimers,
717 C. 2020. Analysis of hydraulic fracturing on the 4100 level at the Sanford Underground
718 Research Facility. Paper presented at the 54th U.S. Rock Mechanics/Geomechanics
719 Symposium, physical event cancelled.
720 Kneafsey, T. J., Dobson, P. F., Ajo-Franklin, J. B. et al. (2019). EGS Collab Project: status, tests,
721 and data. Paper presented at Proceedings of the 53rd US Rock Mechanics/Geomechanics
722 Symposium, New York City, United States.
723 Li, W., Frash, L., Welch, N., Carey, J. W., Meng, M., & Wigand, M. (2021). Stress-Dependent
724 Fracture Permeability Measurements and Implications for Shale Gas Production. *Fuel*.
725 2021: 119984.
726 Liang, F., Sayed, M., Al-Muntasheri, G. A., Chang, F. F., & Li, L. (2016). A comprehensive review
727 on proppant technologies. *Petroleum*, 2(1), 26-39.
728 Leeman, J. R., Saffer, D. M., Scuderi, M. M., & Marone, C. (2016). Laboratory observations of
729 slow earthquakes and the spectrum of tectonic fault slip modes. *Nature communications*,
730 7(1): 1-6.
731 Marone, C., & Kilgore, B. (1993). Scaling of the critical slip distance for seismic faulting with
732 shear strain in fault zones. *Nature*, 362(6421): 618-621.
733 McClure, M. W., & Horne, R. N. (2014a). Characterizing hydraulic fracturing with a tendency for
734 shear stimulation test. Paper presented at SPE Annual Technical Conference and
735 Exhibition, New Orleans, United States.
736 McClure, M.W., & Horne, R.N. (2014b). An investigation of stimulation mechanisms in Enhanced
737 Geothermal Systems. *International Journal of Rock Mechanics and Mining Sciences*. 72:
738 242-260.
739 Morris, J.P. (2021) FatCrayonToolkit. https://github.com/joepmorris/FatCrayonToolkit.
740 Kluge, C., Blöcher, G., Barnhoorn, A., & Bruhn, D. (2020). Hydraulic-mechanical properties of
741 microfaults in granitic rock using the Punch-Through Shear test. *International Journal of*
742 *Rock Mechanics and Mining Sciences*, 134: 104393.

Kluge, C., Blöcher, G., Barnhoorn, A., Schmittbuhl, J., & Bruhn, D. (2021). Permeability evolution during shear zone initiation in low-porosity rocks. *Rock Mechanics and Rock Engineering*. 54, 5221–5244.

Nemoto, K., Moriya, H., Niitsuma, H., & Tsuchiya, N. (2008). Mechanical and hydraulic coupling of injection-induced slip along pre-existing fractures. *Geothermics*, 37(2): 157-172.

Oohashi, K., Hirose, T., & Shimamoto, T. (2013). Graphite as a lubricating agent in fault zones: An insight from low-to high-velocity friction experiments on a mixed graphite-quartz gouge. *Journal of Geophysical Research: Solid Earth*, 118(5), 2067-2084.

Pandey, S. N., Vishal, V., & Chaudhuri, A. (2018). Geothermal reservoir modeling in a coupled thermo-hydro-mechanical-chemical approach: a review. *Earth-Science Reviews*, 185, 1157-1169.

Pyrak-Nolte, L.J. and Morris, J.P (2000) Single fractures under normal stress: The relation between fracture specific stiffness and fluid flow. *International Journal of Rock Mechanics and Mining Sciences*, 37: 245-262.

Renshaw C. E. (1995). On the relationship between mechanical and hydraulic apertures in rough-walled fractures. *Journal of Geophysical Research: Solid Earth*, 100(B12): 24629–24636. https://doi.org/10.1029/95JB02159.

Roggenthen, W. M. (2017). Geophysical and Geological Characterization of Core Materials in Support of the kISMET Experiment at the Sanford Underground Research Facility (SURF). Paper presented at 51st US Rock Mechanics/Geomechanics Symposium. San Francisco, Unites States.

Rutqvist, J., Figueiredo, B., Hu, M., & Tsang, C. F. (2018). Continuum modeling of hydraulic fracturing in complex fractured rock masses. In Hydraulic Fracture Modeling (pp. 195-217). Gulf Professional Publishing.

Sánchez-Roa, C., Faulkner, D. R., Boulton, C., Jimenez-Millan, J., & Nieto, F. (2017). How phyllosilicate mineral structure affects fault strength in Mg-rich fault systems. *Geophysical Research Letters*, 44(11): 5457-5467.

Schultz, R. A., Soliva, R., Fossen, H., Okubo, C. H., & Reeves, D. M. (2008). Dependence of displacement–length scaling relations for fractures and deformation bands on the volumetric changes across them. *Journal of Structural Geology*. 30: 1405–1411.

Singh, A., Neupane, G., Dobson, P., et al. (2019). Slip Tendency Analysis of Fracture Networks to Determine Suitability of Candidate Testbeds for the EGS Collab Hydroshear Experiment. Idaho National Lab., Idaho Falls, United States.

Tester, J.W., et al. (2006). The Future of Geothermal Energy: Impact of Enhanced Geothermal Systems (EGS) on the United States in the 21st Century. U. S. Department of Energy.

Ulrich, C., Dobson, P. F., Kneafsey, T. J., Roggenthen, W. M., Uzunlar, N., Doe, T. W., ... & Singh, A. (2018, June). The distribution, orientation, and characteristics of natural fractures for Experiment 1 of the EGS Collab Project, Sanford Underground Research Facility. In 52nd US Rock Mechanics/Geomechanics Symposium, Seattle, Washington.

Vogler, D., Amann, F., Bayer, P., & Elsworth, D. (2016) Permeability evolution in natural fractures subject to cyclic loading and gouge formation. *Rock Mechanics and Rock Engineering* 49: 3463-3479.

Wenning, Q. C., Madonna, C., Kurotori, T., & Pini, R. (2019). Spatial Mapping of Fracture Aperture Changes With Shear Displacement Using X‐ray Computerized Tomography. Journal of Geophysical Research: Solid Earth, 124(7), 7320-7340.

Wenning, Q. C., Madonna, C., Kurotori, T., Petrini, C., Hwang, J., Zappone, A., Wiemer, S., Giardini, D., Pini, R. (2021). Chemo-Mechanical Coupling in Fractured Shale With Water and Hydrocarbon Flow. Geophysical Research Letters, 48(5), e2020GL091357.

Wu, W., Reece, J. S., Gensterblum, Y., & Zoback, M. D. (2017). Permeability evolution of slowly slipping faults in shale reservoirs. *Geophysical Research Letters*, 44(22): 11-368.

Witherspoon PA, Wang JS, Iwai K, Gale JE. (1980). Validity of cubic law for fluid flow in a deformable rock fracture. *Water Resources Research,* 16(6): 1016–1024.

Xiong, X., Li, B., Jiang, Y., Koyama, T., & Zhang, C. (2011). Experimental and numerical study of the geometrical and hydraulic characteristics of a single rock fracture during shear. *International Journal of Rock Mechanics and Mining Sciences*, 48(8): 1292-1302.

Ye, Z., & Ghassemi, A. (2018). Injection-induced shear slip and permeability enhancement in granite fractures. *Journal of Geophysical Research: Solid Earth*, 123(10): 9009-9032.

Ye, Z., & Ghassemi, A. (2019). Injection-induced propagation and coalescence of preexisting fractures in granite under triaxial stress. *Journal of Geophysical Research: Solid Earth*, 124(8), 7806-7821.

Ye, Z., & Ghassemi, A. (2020). Heterogeneous fracture slip and aseismic-seismic transition in a triaxial injection test. *Geophysical Research Letters*, 47(14), e2020GL087739.

Zimmerman, R. W., & Bodvarsson, G. S. (1996). Hydraulic conductivity of rock fractures. *Transport in Porous Media*, 23(1): 1-30.

Zhang, Q., Li, X., Bai, B., Pei, L., Shi, L., & Wang, Y. (2019). Development of a direct-shear apparatus coupling with high pore pressure and elevated temperatures. *Rock Mechanics and Rock Engineering*, 52(9): 3475-3484.

Tables

Table 1. In-situ stress, lab testing conditions, and natural fracture orientations of the EGS Collab sites.

In-situ stress of EGS Collab testbeds using information available at time of testing						
Location	Rock type		Depth (m)	Sv (MPa)	SH (MPa)	Sh (MPa)
E1 4850 level *	Schist (PS01)		1480	44.1	42.6	21.7
E2 4100 level *	Amphibolite and Rhyolite (YA02)		1250	36	37.3	18.3
Laboratory testing conditions to simulate in-situ stresses						
Location	$\frac{\sigma_1 - \sigma_3}{2}$	$\frac{\sigma_1 + \sigma_3}{2}$	τ_n at 30° from σ_1	σ_n at 30° from σ_1		
E1 4850 level *	10.45	32.15	9	27		
E2 4100 level *	9.5	27.8	8.2	23		
E1 4850 level **	10	34	8.7	29		
E2 4100 level **	9	27	7.7	23		

Natural fracture orientations of EGS Collab field sites										
Location	Hydraulic fracture		Joint set 1		Joint set 2		Joint set 3		Foliation (also Joint set 4 for E1)	
	Strike	Dip	Strike	Dip	Strike	Dip	Strike	Dip	Strike	Dip
E1 4850 level	86°	78°	237°	84°	10°	33°	227°	19°	145°	80°
E2 4100 level	104°	63°	15°	35°	260°	69°	120°	35°	120°	35°

* The most recent values available;

** Values used for laboratory experiments based on the data that was available at the time of testing. The difference in laboratory testing conditions is trivial.

817 Table 2. Specimen prepared for triaxial direct shear experiments

Specimen	Field site	Rock Type	Orientation	Character
PS01-03	E1	Schist	Sub-parallel to the E1-foliation	Mineral infilled fracture
PS01-06	E1	Schist	Sub-parallel to E1-JS2	Mineral infilled fracture
PS01-08	E1	Schist	Sub-parallel to E1-JS1	Mineral infilled fracture
PS01-09	E1	Schist	Sub-parallel to E1-JS3	Mineral infilled fracture
PS01-11	E1	Schist	Sub-parallel to the E1-JS4 and foliation	Opening-mode, weak fracture
YA02-01	E2	Amphibolite/rhyolite	Sub-parallel to E2-JS1	Amphibolite/rhyolite contact with visible pores
YA02-02	E2	Amphibolite	Sub-parallel to E2-JS2	Mineral infilled fracture
YA02-03	E2	Amphibolite	Sub-parallel to E2-JS2	Mineral infilled fracture
YA02-04	E2	Rhyolite	Sub-parallel to E2-JS3 and foliation	Mineral infilled fracture
YA02-05	E2	Rhyolite	Equally sub-parallel to the E2-JS3 & foliation and minimum principal stress	Opening-mode, weak infilled fracture

818

819
820 Table 3. X-ray powder diffraction analysis of crystalline rock fracture infilling materials.

	Poorman Schist					Yates Amphibolite				
	PS 01-03	PS 01-06	PS 01-08	PS 01-09	PS 01-11	YA 02-01	YA 02-02	YA 02-03	YA 02-04	YA 02-05
Tectosilicate										
Plagioclase	-	2.7	1.1	1.5	-	22.3	16.9	12.4	-	-
K-Feldspar	-	4.1	4.5	2.5	-	4.9	-	7.8	69.1	58.2
Quartz	19.9	25.9	28.5	26.4	11.0	12.3	8.5	24.5	26.7	30.8
TOTAL	19.9	32.7	34.1	30.4	11	39.5	25.4	44.7	95.8	89.0
Carbonate mineral										
Calcite	15.3	2.5	0.2	0.5	2.0	0.7	2.8	8.9	-	4.6
Dolomite	32.1	39.2	43.4	40.7	2.3	14.7	-	4.1	3.1	2.1
TOTAL	47.4	41.7	43.6	41.2	4.3	15.4	2.8	13	3.1	6.7
Sulfate minerals										
Gypsum	-	4.1	8.5	6.3	0.7	-	-	-	-	-
Pyrite	-	0.9	0.5	0.5	-	7.0	-	-	1.2	1.8
Sphalerite	-	-	-	-	-	6.2	1.3	-	-	1.0
Galena	-	-	-	-	-	2.2	-	-	-	1.5
TOTAL		5	9	6.8	0.7	15.4	1.3	--	1.2	4.3
Native mineral										
Graphite	2.3	2.1	1.5	0.5	6.7	-	-	-	-	-
TOTAL	2.3	2.1	1.5	0.5	6.7	-	-	-	-	-
Inosilicate mineral										
Amphibole	-	-	-	-	-	26.5	59.0	25.5	-	-
TOTAL	-	-	-	-	-	26.5	59.0	25.5	-	-
Phyllosilicate (Sheet Silicate minerals)										
Annite	-	0.3	0.0	1.2	3.4	-	-	-	-	-
Muscovite	24.4	18.1	11.8	19.9	54.8	-	5.9	0.6	-	-
Chlorite	4.3	-	-	-	19.2	3.2	5.6	16.2	-	-
Kaolinite	1.8	-	-	-	-	-	-	-	-	-
TOTAL	30.5	18.4	11.8	21.1	77.3	3.2	11.5	16.8	0.0	0.0
GRAND TOTAL	100.0	100.0	100.0	100.0	100.0	100.0	100.0	100.0	100.0	100.0

821

Table 4. Measured shear strength, permeability enhancement of natural fractures.

Field sites	Specimen	Intact shear strength at in-situ normal stress	Friction angle and cohesion for the fracture	Theoretical hydroshearing fluid pressure	Actual hydroshearing fluid pressure	Phyllosilicate Content of fractures	Intact permeability	Fracture permeability		Hydroshearing		Maximum pore pressure *
								After mechanical shear	After hydroshear	Before mechanical shear	After mechanical shear	
E1 Site 4850 level	PS01-03	25 MPa	41.4 (±0.08) ° 3.8 (±0.04) MPa	23.2 (±0.1) MPa	23 MPa	30.5%	$<10^{-4}$ mD	0.2-0.4 mD	0-5 mD	No	Yes	28.5 MPa
	PS01-06	45 MPa	36 (±1) ° 3.24 (±0.6) MPa	22 (±1) MPa	23.5 MPa	18.4%	$<10^{-4}$ mD	0.01-0.1 mD	0.1-1 mD	No	Yes	
	PS01-08	59 MPa	41.8 (±0.6) ° 4.3 (±0.5) MPa	24 (±0.6) MPa	--	11.8%	$<10^{-3}$ mD	0.3-1.2 mD	4-7 mD	No	Yes	
	PS01-09	66 MPa	29.1 (±5) ° 20 (±5) MPa	49 (±3) MPa	Did not occur	21.1%	10^{-4}-10^{-3} mD	0.002-0.008 mD	0.001-0.56 mD	No	No	
	PS01-11	11 MPa	17 (±0.5) ° 1.9 (±0.5) MPa	6 (±2.5) MPa	7.4 MPa	77.3%	0.2-0.3 mD	0.02-0.03 mD	0.002-0.01 mD	Yes	Yes	
E2 Site 4100 level	YA02-01	50 MPa	--	--	Did not occur	3.2%	10^{-4}-10^{-3} mD	0.01-8 mD	--	No	--	22.5 MPa
	YA02-02	42 MPa	38.1 (±0.03) ° 4.1 (±0.04) MPa	18 (±0.06) MPa	--	11.5%	10^{-4}-10^{-3} mD	0.01-0.13 mD	--	--	--	
	YA02-03	27 MPa	24.1 (±0.24) ° 4.4 (±0.18) MPa	15.3 (±0.5) MPa	--	16.8%	10^{-4}-10^{-3} mD	0.0003-0.002 mD	--	--	--	
	YA02-04	34 MPa	35.4 (±0.12) ° 6.8 (±0.1) MPa	21.4 (±0.1) MPa	--	0	10^{-4}-10^{-3} mD	0.1-0.3 mD	--	--	--	
	YA02-05	23 MPa	39.7 (±0.5) ° 2.8 (±0.5) MPa	16.7 (±0.7) MPa	17.8-19.7 MPa	--	0.3-0.35 mD	0.6-6 mD	0.3-0.9	Yes	Yes	

* Maximum pore pressure is 0.5 MPa lower than the confining pressure of the experiment.

Table 5. Fitted parameters relating confining stress, mechanical aperture, and hydraulic aperture.

Specimen ID		Barton-Bandis model				Exponential model			Modified Witherspoon factor N		
		b_{b0} (mm)	A (mm/N)	B (N^{-1})	R^2	b_{e0} (mm)	α (MPa^{-1})	R^2	Regression value	Uncertainty	R^2
PS01-06	Unloading	0.8220± 3.00e-3	0.0355± 4.41e-4	0.0432± 3.79e-4	1.00	0.7405± 1.67e-3	0.0254± 1.25e-4	1.00	0.0078	0.0070~ 0.0088	0.96
PS01-11	Unloading	0.6711± 1.79e-2	0.0035± 3.83e-3	0.0515± 4.34e-3	0.99	0.6313± 1.02e-2	0.0324± 1.42e-3	1.00	0.0023	0.0021~ 0.0026	0.79
YA02-02	Loading	0.1388± 3.30e-4	0.0034± 2.86e-5	0.0248± 1.47e-4	1.00	0.1257± 1.49e-4	0.0145± 3.78e-5	1.00	0.0388	0.0453~ 0.0360	0.74
	Unloading	0.0839± 8.66e-5	0.0008± 4.44e-6	0.01± 4.27e-5	1.00	0.0814± 1.26e-4	0.0076± 4.54e-5	0.99	0.0400	0.0447~ 0.0376	0.72
YA02-03	Loading	0.1710± 3.94e-4	0.0030± 2.81e-5	0.0174± 1.24e-4	0.99	0.1622± 5.21e-5	0.0118± 1.05e-5	1.00	0.0097	0.0107~ 0.0864	0.87
	Unloading	0.1416± 8.54e-5	0.0018± 5.22e-6	0.0129± 2.91e-5	1.00	0.1369± 1.48e-4	0.0094± 3.47e-5	1.00	0.0086	0.0099~ 0.0055	0.84
YA02-04	Loading	0.2033± 3.70e-4	0.0031± 2.36e-5	0.0153± 8.82e-5	1.00	0.1938± 9.86e-5	0.0105± 1.50e-5	1.00	0.0281	0.0321~ 0.0261	0.69
	Unloading	0.1608± 1.83e-4	0.0014± 6.18e-6	0.0097± 5.28e-5	1.00	0.1583± 2.67e-4	0.0076± 5.52e-5	0.99	0.0296	0.0349~ 0.0267	0.79
YA02-05	Loading	0.7178± 6.29e-3	0.280± 7.72e-4	0.0390± 7.34e-4	0.86	0.6629± 2.46e-3	0.0226± 1.41e-4	0.96	--	--	--
	Unloading	0.6232± 6.55e-3	0.034± 1.03e-3	0.0552± 1.07e-3	0.90	0.5277± 1.56e-3	0.0262± 1.14e-4	0.98	--	--	--

Figures

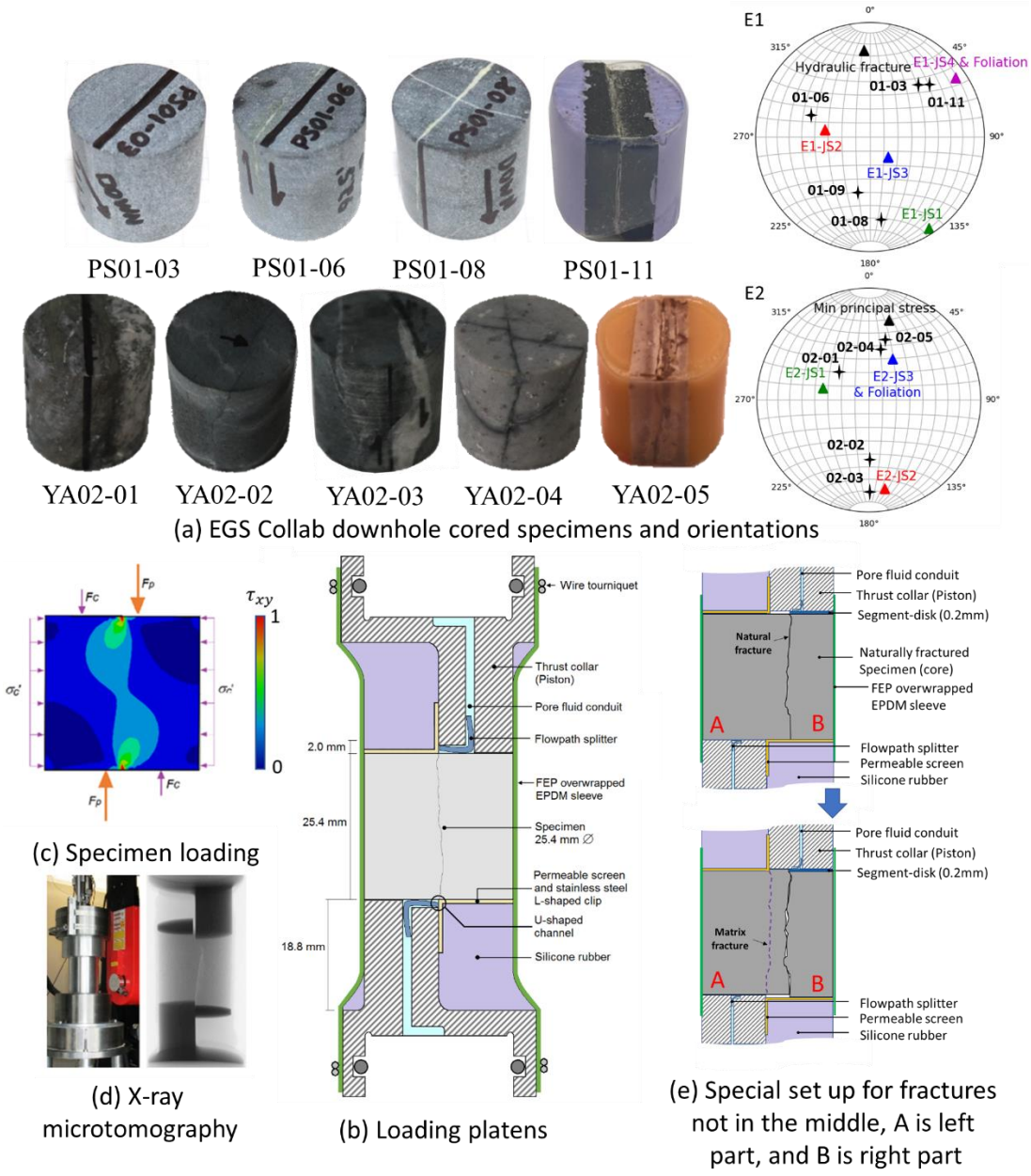

Figure 1. Triaxial direct-shear setup and crystalline specimens drilled from EGS Collab field sites. (a) Care was taken to orient cores parallel to natural fractures and to position the fracture across the diameter of the core, making these specimens ideal for triaxial direct-shear testing that targeted suspected weak natural fractures. The orientations of each specimen and major joint sets are presented in the hemisphere plot achieved from optical and acoustic televiewer borehole logging images. The triangle markers represent the poles to the planes for major joint sets, while the star markers represent the poles to the planes for specimens. (b) The naturally fractured specimen is aligned with the direct-shear plane produced by the two opposing half-cylinder pistons. (c) The stress distribution of the specimen during the experiment predicted by Abaqus modeling (Frash et al., 2016, 2019a). (d) X-ray imaging setup and greyscale radiograph during an experiment. (e) A stainless steel segment-disk was inserted when needed to ensure initial shear loading across the targeted natural fracture (e.g., YA02-02).

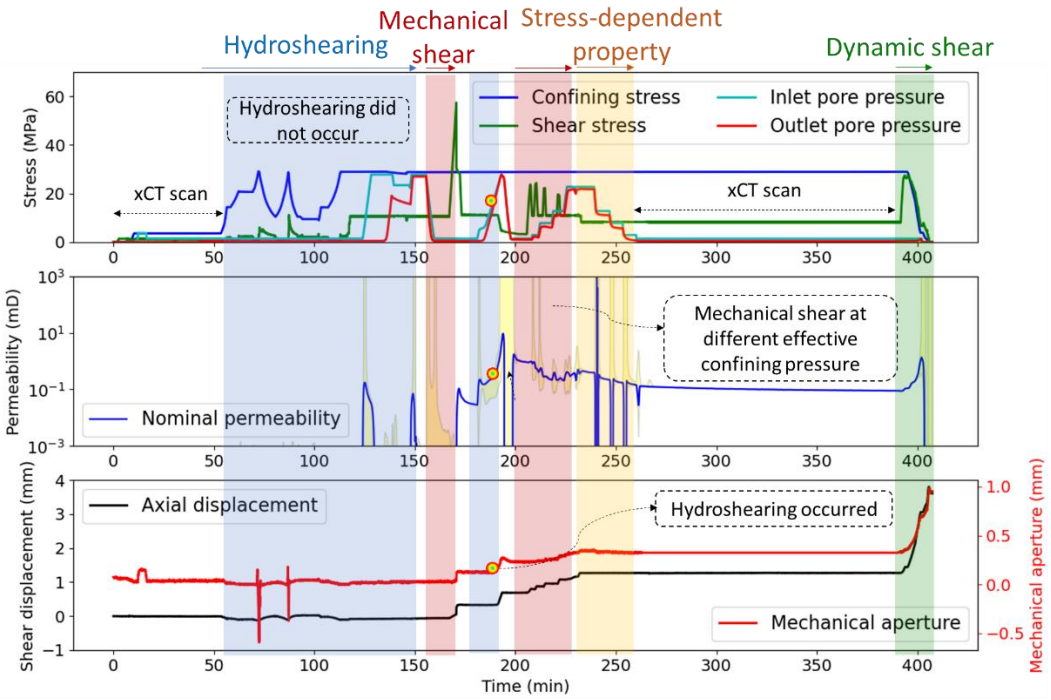

(a) Hydromechanical measurement of PS01-06

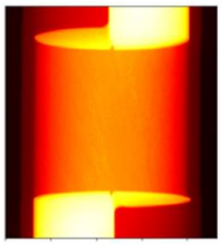

(b) Original sample at 45 min

(c) After hydroshearing at 161 min

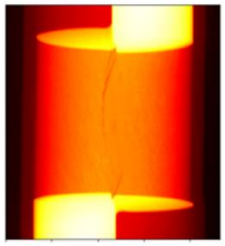

(d) After mechanical at 173 min

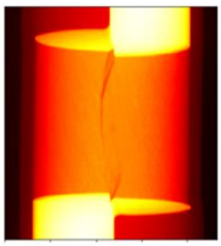

(e) After hydroshearing at 197 min

(f) Before dynamic shear at 390.6 min

(g) After dynamic shear at 405 min

Figure 2. Hydro-mechanical measurement of PS01-06 and in-situ x-ray imaging. (a) The upper panel shows the pressures as a function of time. The middle panel shows transient permeability, where the yellow color is the uncertainty for the calculated permeability. The bottom panel shows axial displacement and dilation aperture. The highlighted points show the occurrence point of hydroshearing. (b-g) Concurrent radiographs provide confirmation about the geometry of the specimen at uninterrupted in-situ stress conditions. Full 360° CT scans (xCT) were only obtained before and after shearing.

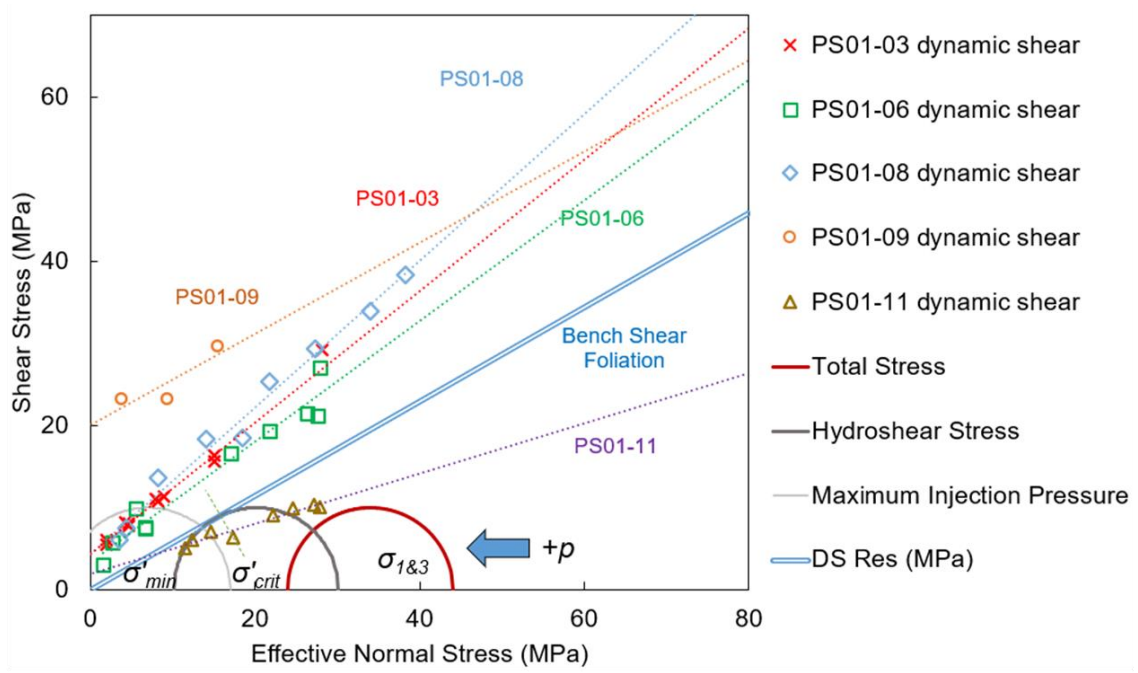

(a) E1 site: 4850 Level

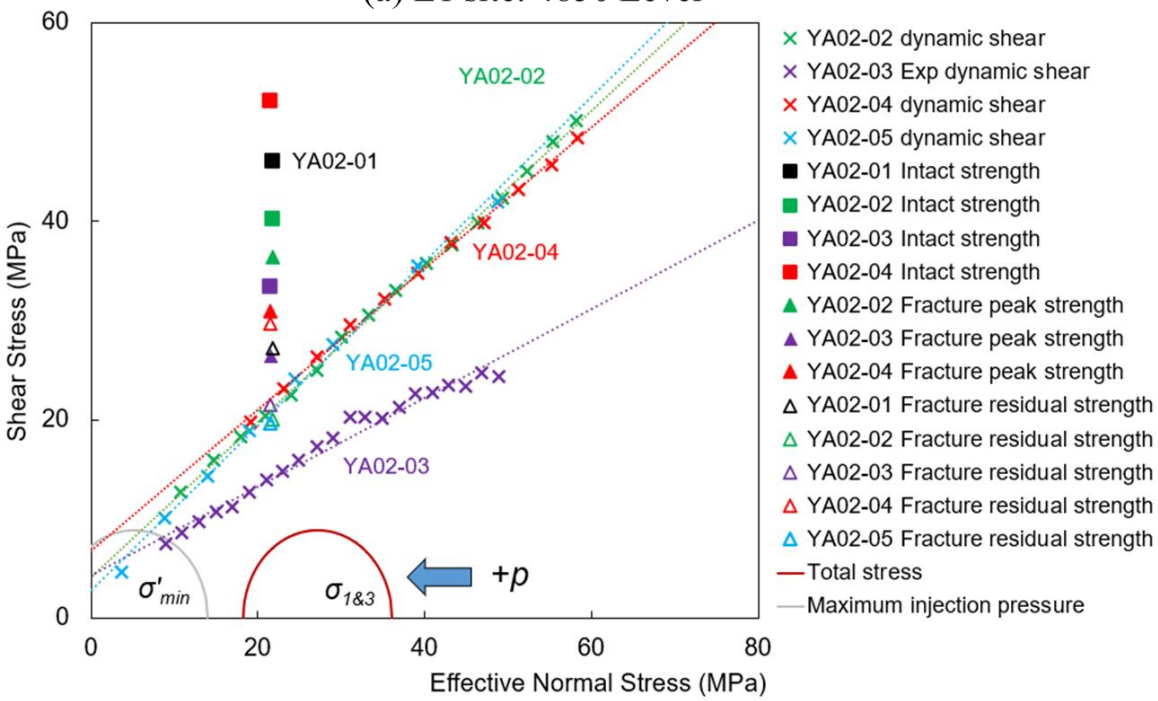

(b) E2 site: 4100 Level

Figure 3. Measured triaxial direct-shear stresses at failure in a Mohr-Coulomb analysis for EGS Collab specimens. Different types of markers represent experimental data during dynamic shear stage for each specimen. The dashed lines are fitted Mohr-Coulomb slip line for each specimen. A benchtop gravity slant shear test was used to estimate a Mohr-Coulomb friction angle of 30° and cohesion of 0 MPa for a separated natural foliation parallel fracture of 4850 level.

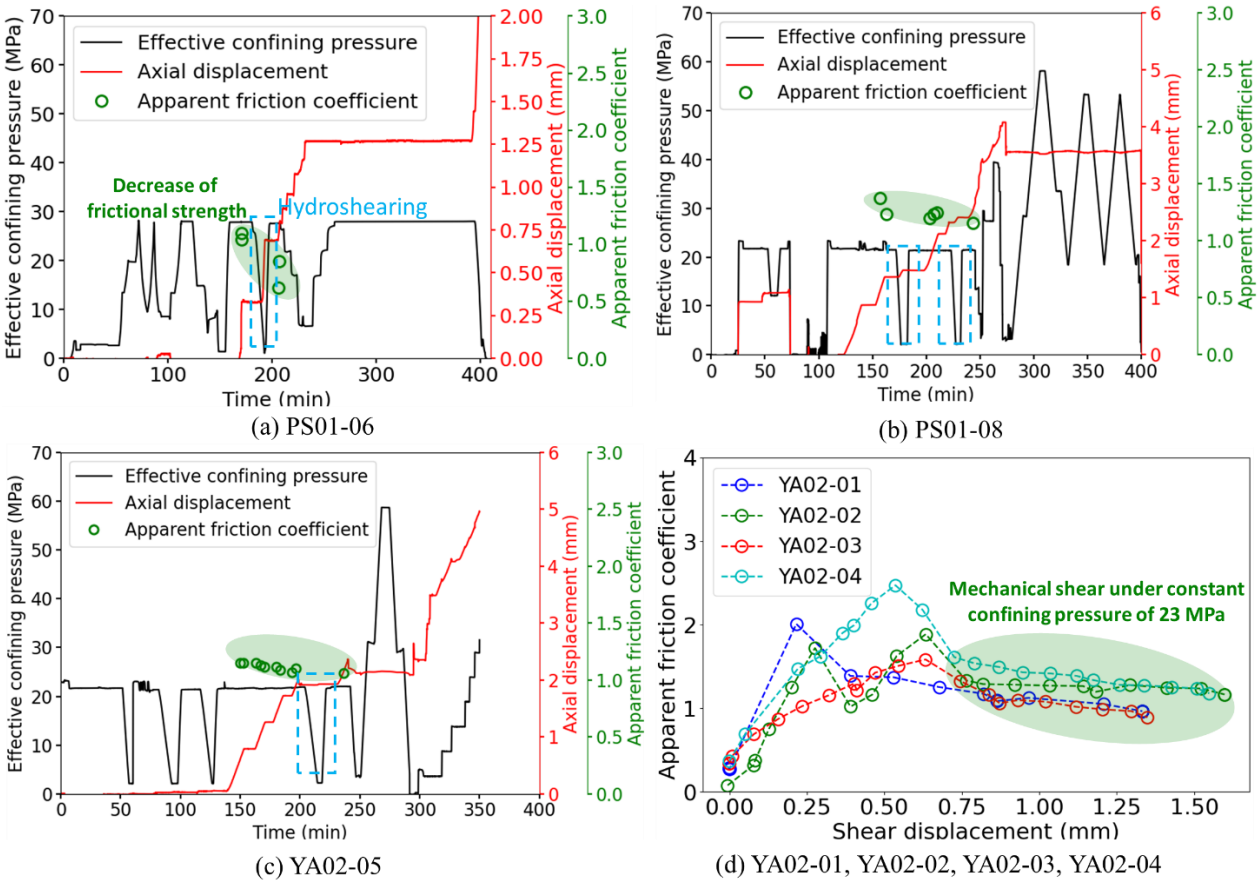

Figure 4. Reduction of apparent frictional coefficient by shearing. The shaded areas in (a), (b), and (c) show the reduction of apparent frictional coefficient after hydroshearing for specimens PS01-06, PS01-08, and YA02-05 respectively. The shaded area in (d) shows frictional strength reduced with more mechanical shear displacement under the same confining stress for specimens YA02-01, YA02-02, YA02-03, and YA02-04.

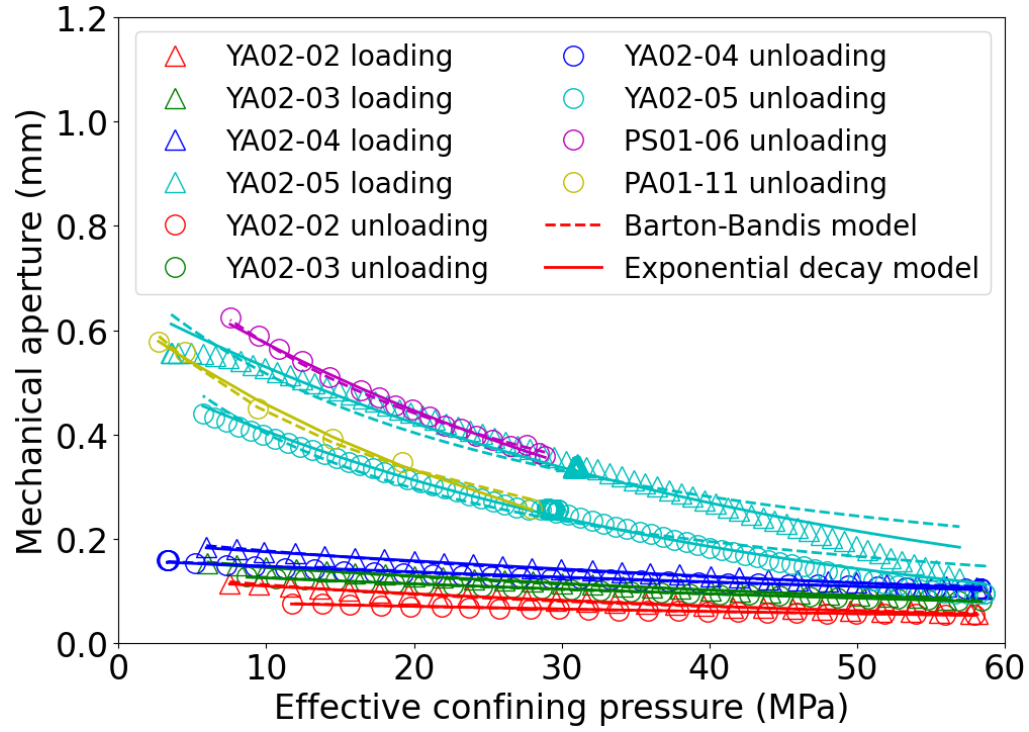

(a)

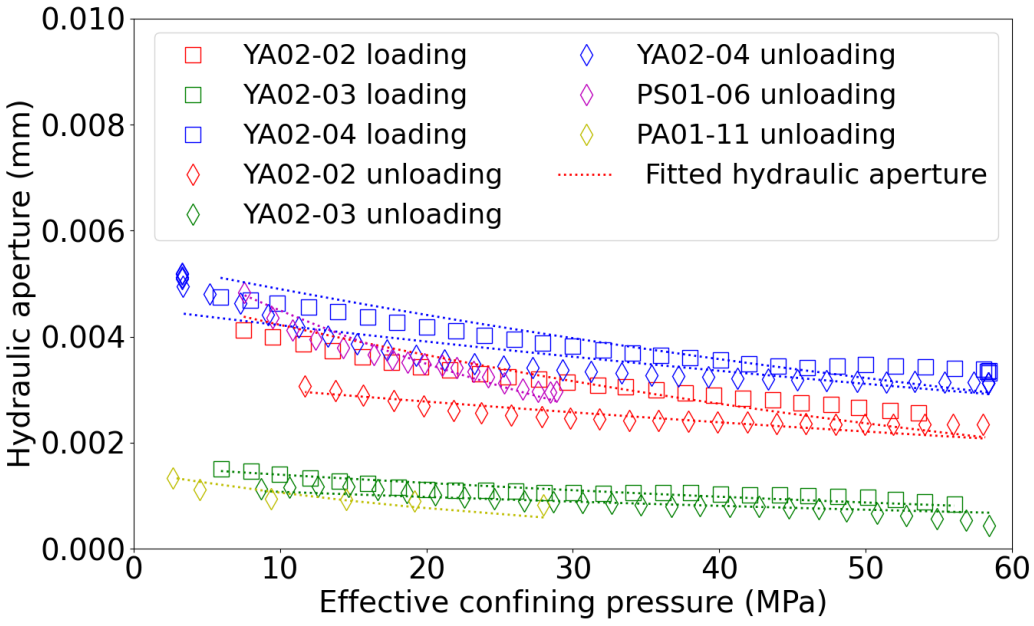

(b)

Figure 5. Relationship between fracture apertures and effective confining pressure. (a) Mechanical aperture versus effective confining pressure. (b) Hydraulic aperture versus effective confining pressure. Curve fitted by Eq. (7) and Eq. (8).

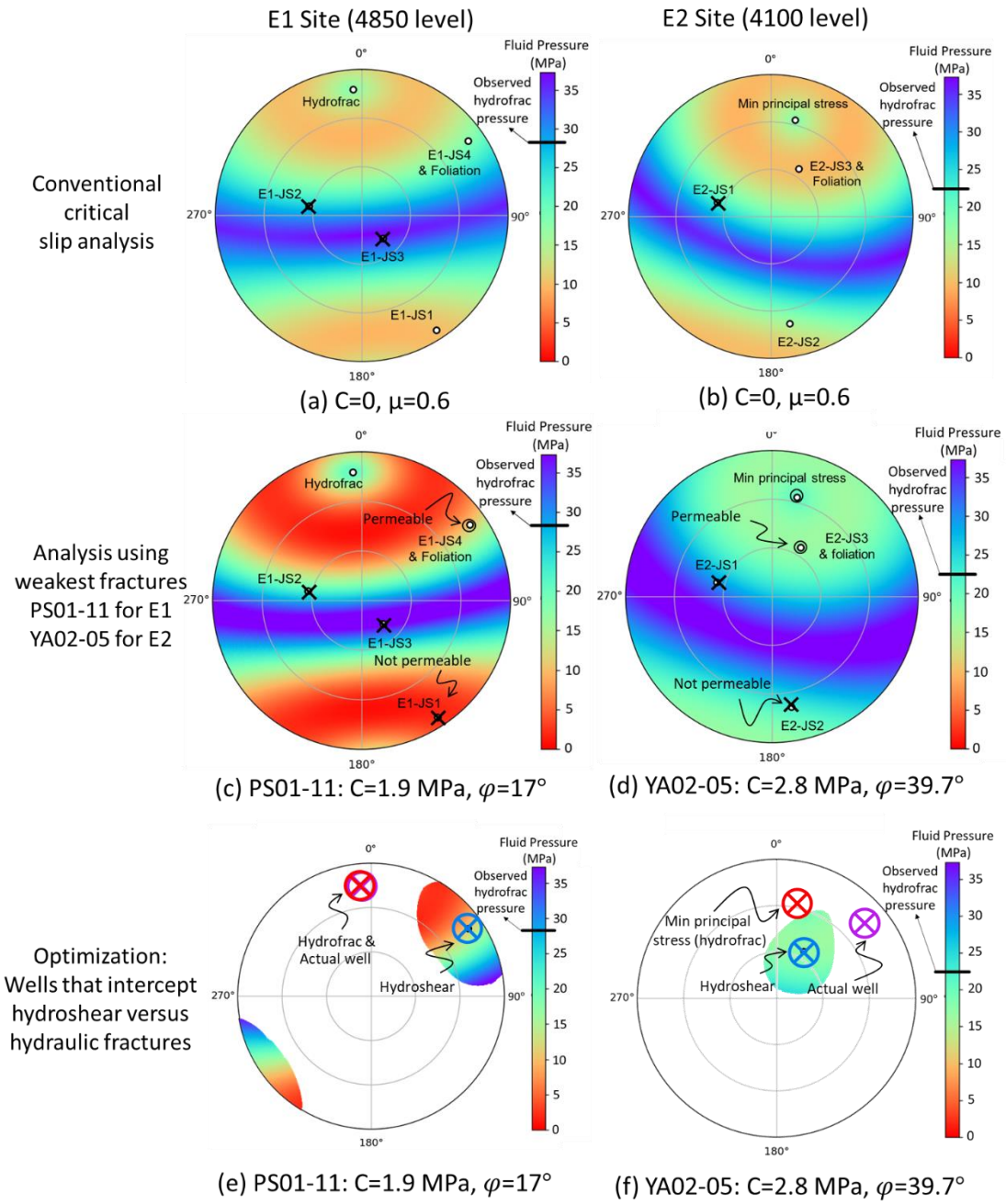

Figure 6. Lower-hemisphere stereoplots of the critical fluid pressure to induce fracture activation (shear or tension) in E1 and E2 site. (a) and (b) shows the conventional critical slip pressure analysis with cohesion of 0 MPa and friction coefficient of 0.6 (Byerlee, 1978) for E1 and E2 site, respectively. Cross symbol means not suitable for hydroshearing. (c) shows the analysis for E1 site assuming the measured weakest fracture strength of PS01-11 with cohesion of 1.9 MPa and friction angle of 17° for all joint sets. (d) shows the analysis for E2 site assuming the measured weakest fracture strength of YA02-05 with cohesion of 2.8 MPa and friction angle of 39.7° for all joint sets. (e) and (f) shows the orientation of the hydraulic fracture, the fracture sets that are best suited for hydroshearing and the actual well placement decision for hydroshearing or hydraulic fracturing in the E1 and E2 sites, respectively. In (e) and (f), color for critical fluid pressure is only shown for orientations within 30° of joint set that the PS01-11 and YA02-05 are sub-parallel to.